Supplementary Information (SI) for Dalton Transactions.
This journal is © The Royal Society of Chemistry 2025

Electronic Supporting Information

Testing mixed metal bimetallic, and monometallic, cryptates for electrocatalytic hydrogen evolution

Varinder Singh,[a] Matthew G. Robb[a] and Sally Brooker[a]*

Department of Chemistry and MacDiarmid Institute for Advanced Materials and Nanotechnology, University of Otago, PO Box 56, Dunedin 9054, New Zealand.

E-mail: sbrooker@chemistry.otago.ac.nz

Table of Contents

1 NMR spectra of the cryptand and the cryptates

1.1 NMR spectrum of the cryptand, L^{i}

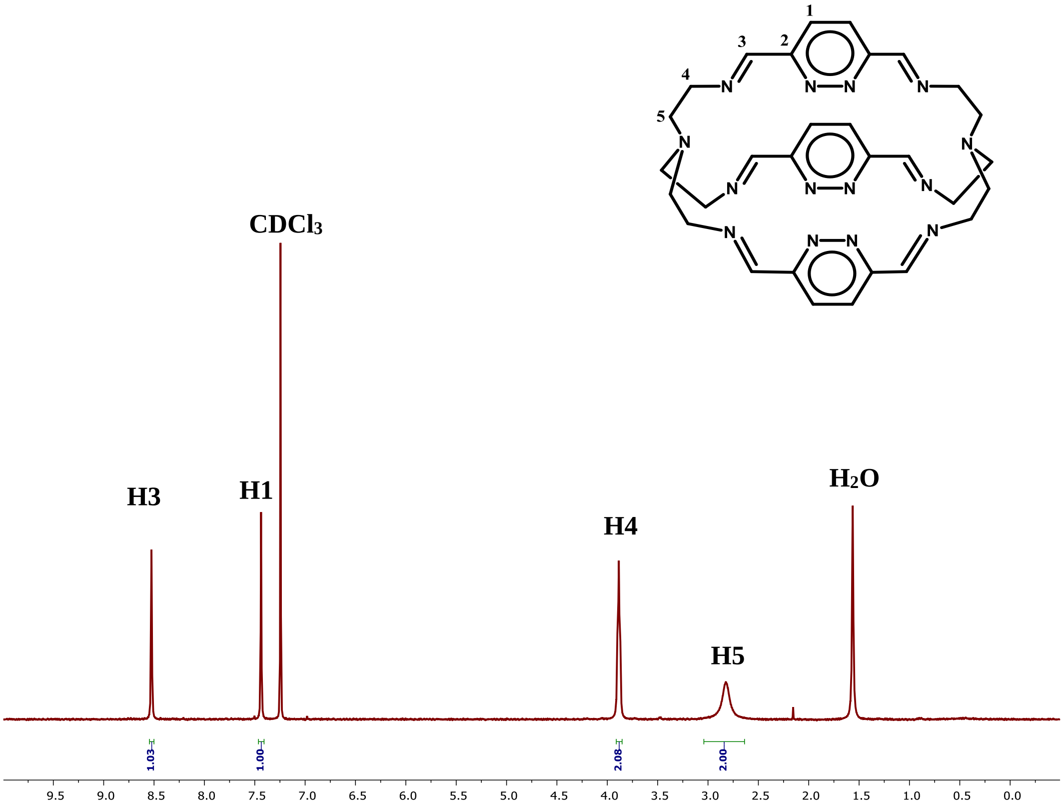

Figure S1. ^{1}H NMR spectrum of the literature macrocyclic ligand, **L**^{i} (400 MHz, CDCl$_3$, 298 K), included here for ease of comparison with the spectra of the new cryptates.

1.2 NMR spectra of the mono-zinc cryptate, [Zn^{II}L^{i}](BF$_4$)$_2$

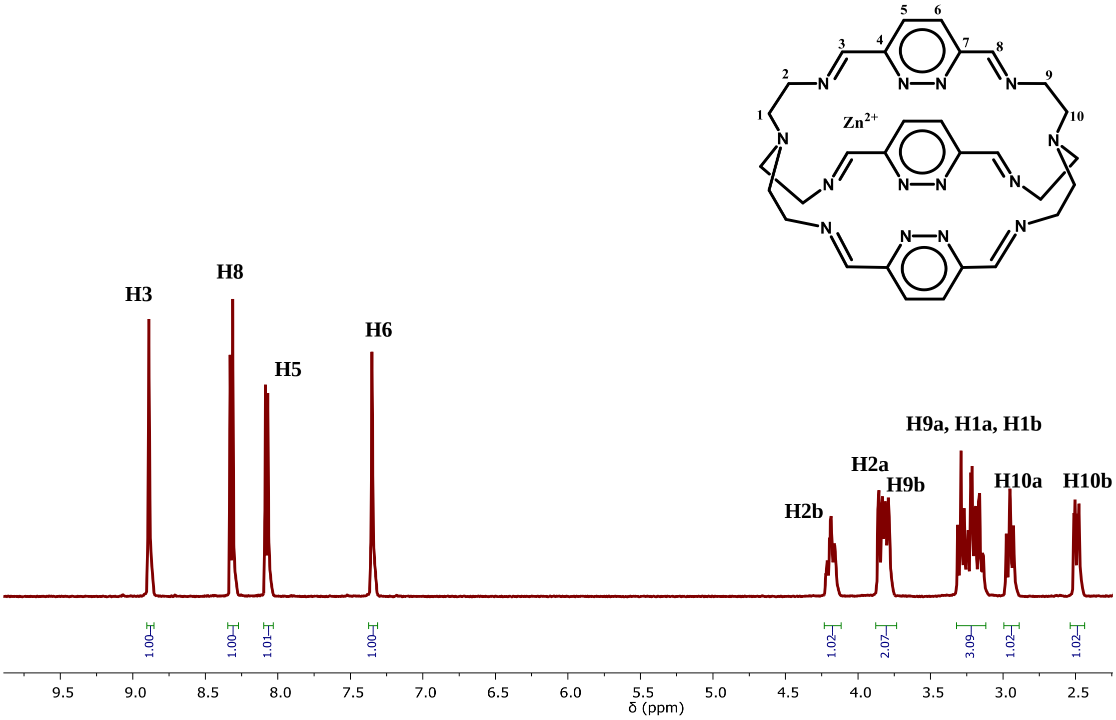

Figure S2. ^{1}H NMR spectrum of [Zn^{II}**L**^{i}](BF$_4$)$_2$.0.5H$_2$O (500 MHz, CD$_3$CN, 298 K). δ (ppm) = 8.89 (m, 1H, H^3), 8.33 (dd, 1H, H^8), 8.08 (tt, 1H, H^5), 7.35 (m, 1H, H^6), 4.18 (tdd, 1H, H^{2b}), 3.83 (m, 2H, H^{2a} and H^{9b}), 3.24 (m, 3H, H^{9a} H^{1a} and H^{1b}), 2.95 (dd, 1H, H^{10a}), 2.50 (m, 1H, H^{10b}).

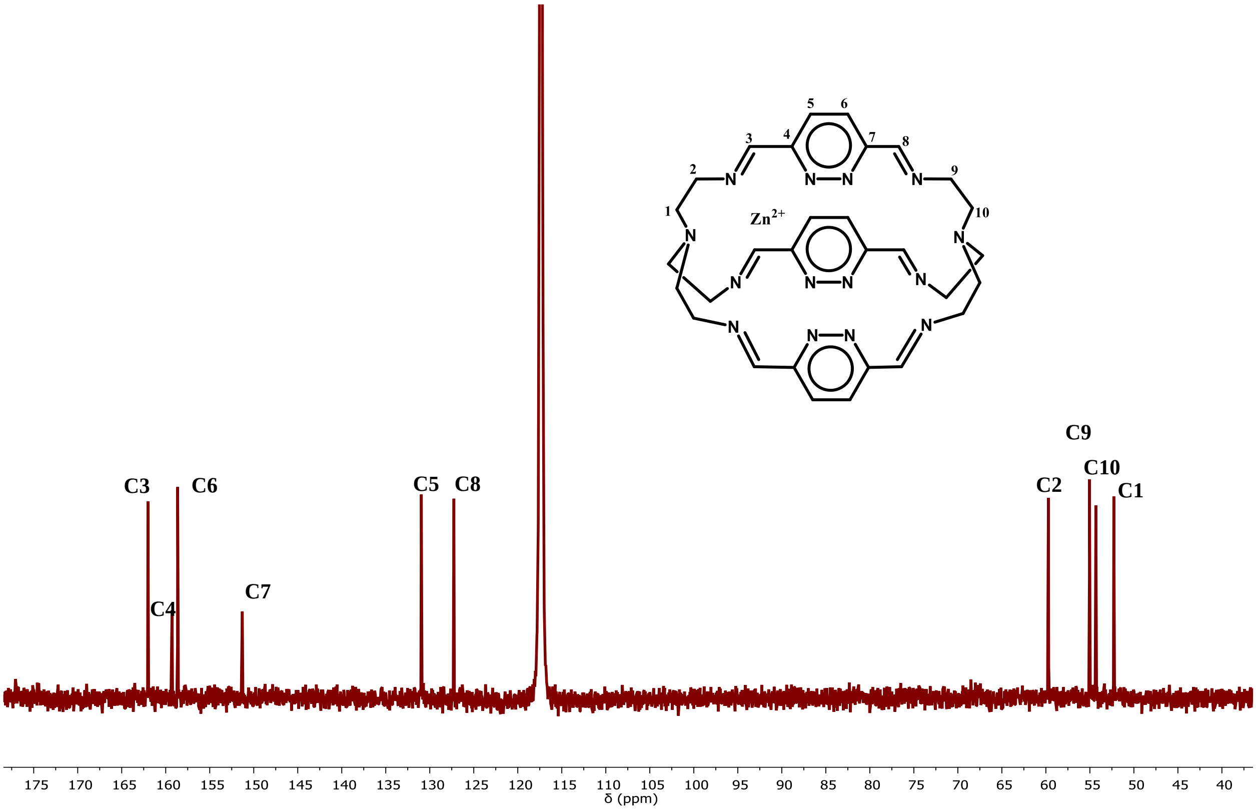

Figure S3. ^{13}C NMR spectrum of [Zn^{II}**L**^{i}](BF$_4$)$_2$.0.5H$_2$O (500 MHz, CD$_3$CN, 298 K). δ = 162.02 (C3), 159.30 (C4), 158.64 (C6), 151.29 (C7), 130.96 (C5), 127.27 (C8), 59.71 (2), 55.05 (C9), 54.32 (C10), 52.28 (C1).

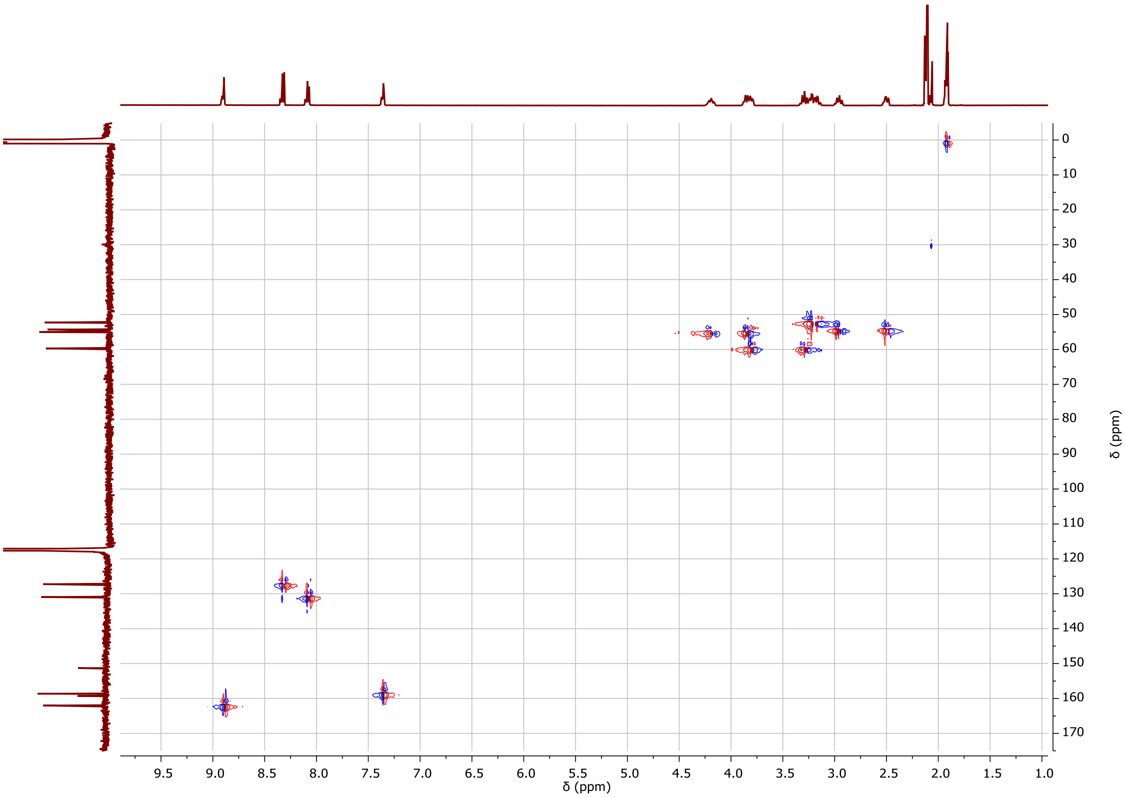

Figure S4. HSQC NMR spectrum of [Zn^{II}**L**^{i}](BF$_4$)$_2$.0.5H$_2$O (500 MHz, CD$_3$CN, 298 K).

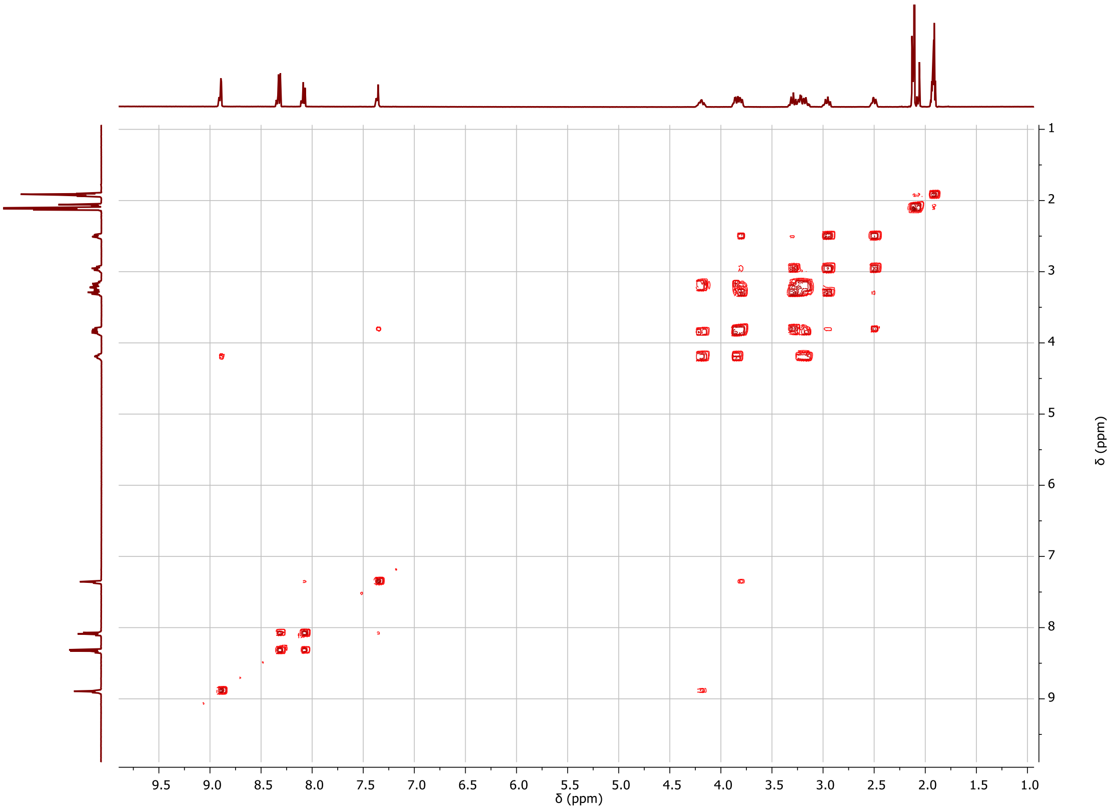

Figure S5. ^{1}H COSY NMR spectrum of [Zn^{II}**L**^{i}](BF$_4$)$_2$.0.5H$_2$O (500 MHz, CD$_3$CN, 298 K).

1.3 NMR spectra of the heterobimetallic cryptate, $[Zn^{II}Cu^{I}L^{i}](BF_4)_3$

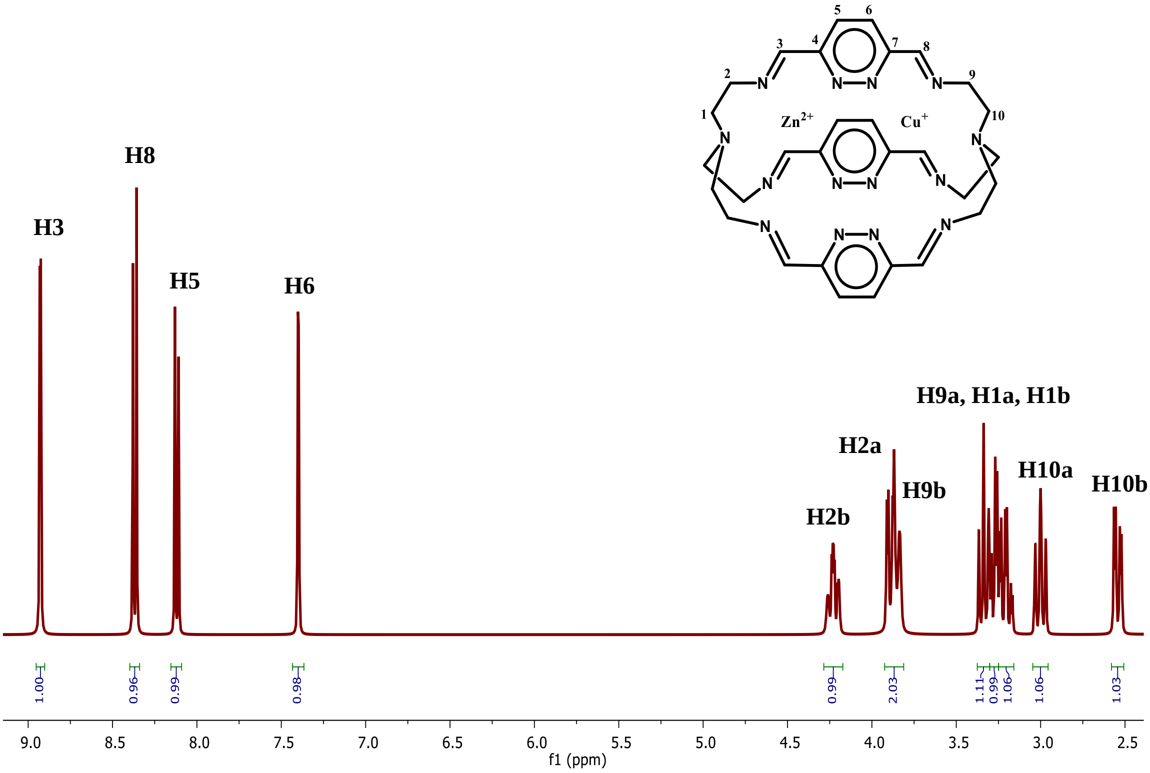

Figure S6. ^{1}H NMR spectrum of $[Zn^{II}Cu^{I}\mathbf{L}^{i}](BF_4)_3$ (500 MHz, solvent CD_3CN, 298 K): 8.93 (d, 1H, H^3), 8.37 (d, 1H, H^8), 8.13 (d, 1H, H^5), 7.40 (s, 1H, H^6), 4.23 (t, 1H, H^{2b}), 3.90 (m, 2H, H^{2a} and H^{9b}), 3.34 (t, 1H, H^{9a}), 3.27 (t, 1H, H^{1a}), 3.21 (td, 1H, H^{1b}), 3.0 (t, 1H, H^{10a}), 2.54 (dd, 1H, H^{10b}).

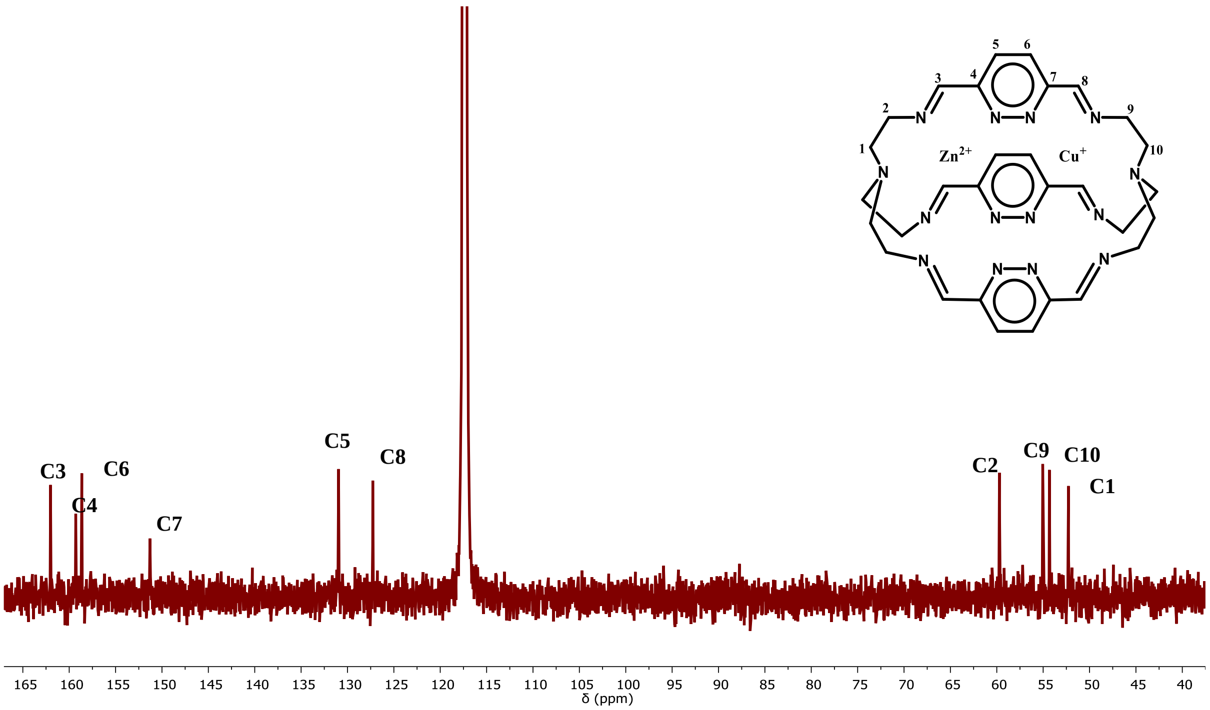

Figure S7. ^{13}C NMR spectrum of [Zn^{II}Cu^{I}**L**^{i}](BF$_4$)$_3$ (500 MHz, CD$_3$CN, 298 K). δ (ppm) = 162.02 (C3), 159.30 (C4), 158.64 (C6), 151.29 (C7), 130.96 (C5), 127.27 (C8), 59.71 (2), 55.05 (C9), 54.32 (C10), 52.28 (C11).

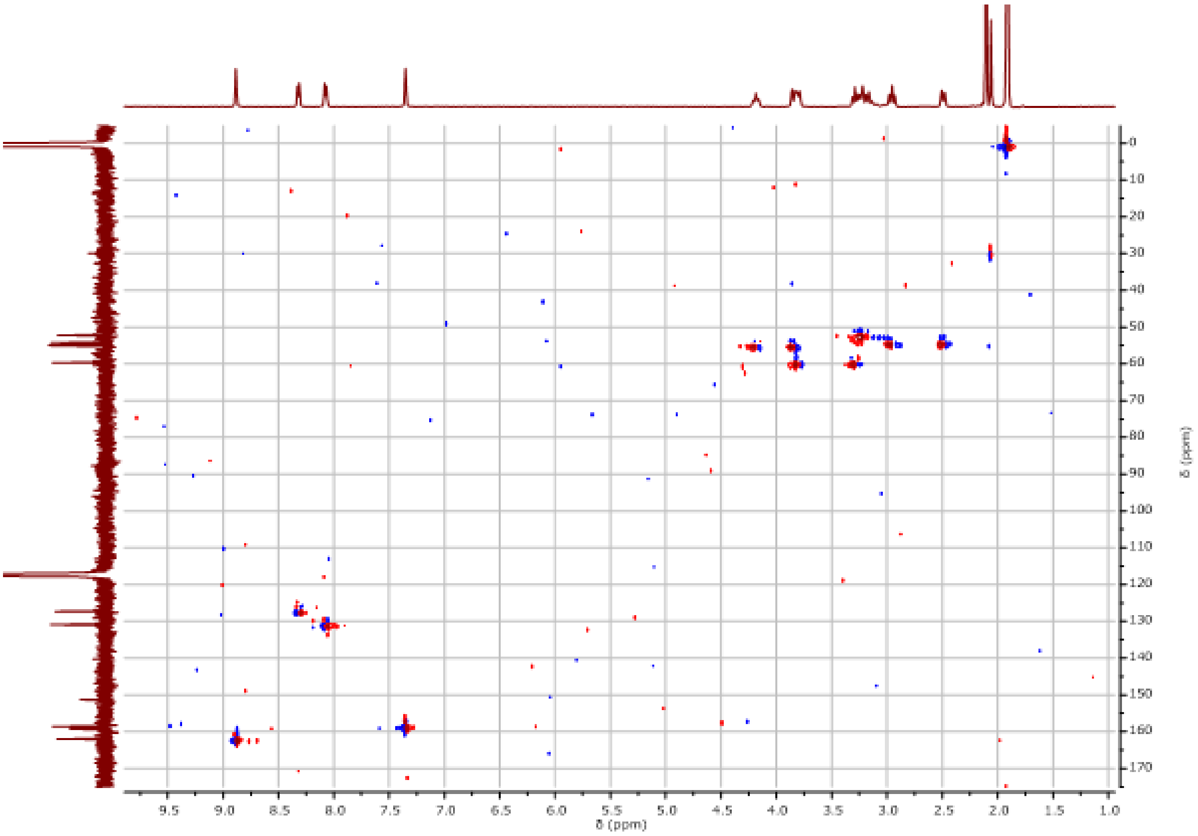

Figure S8. HSQC NMR spectrum of $[\mathrm{Zn^{II}Cu^{I}}\mathbf{L}^{\mathrm{i}}](\mathrm{BF_4})_3$ (500 MHz, CD_3CN, 298 K).

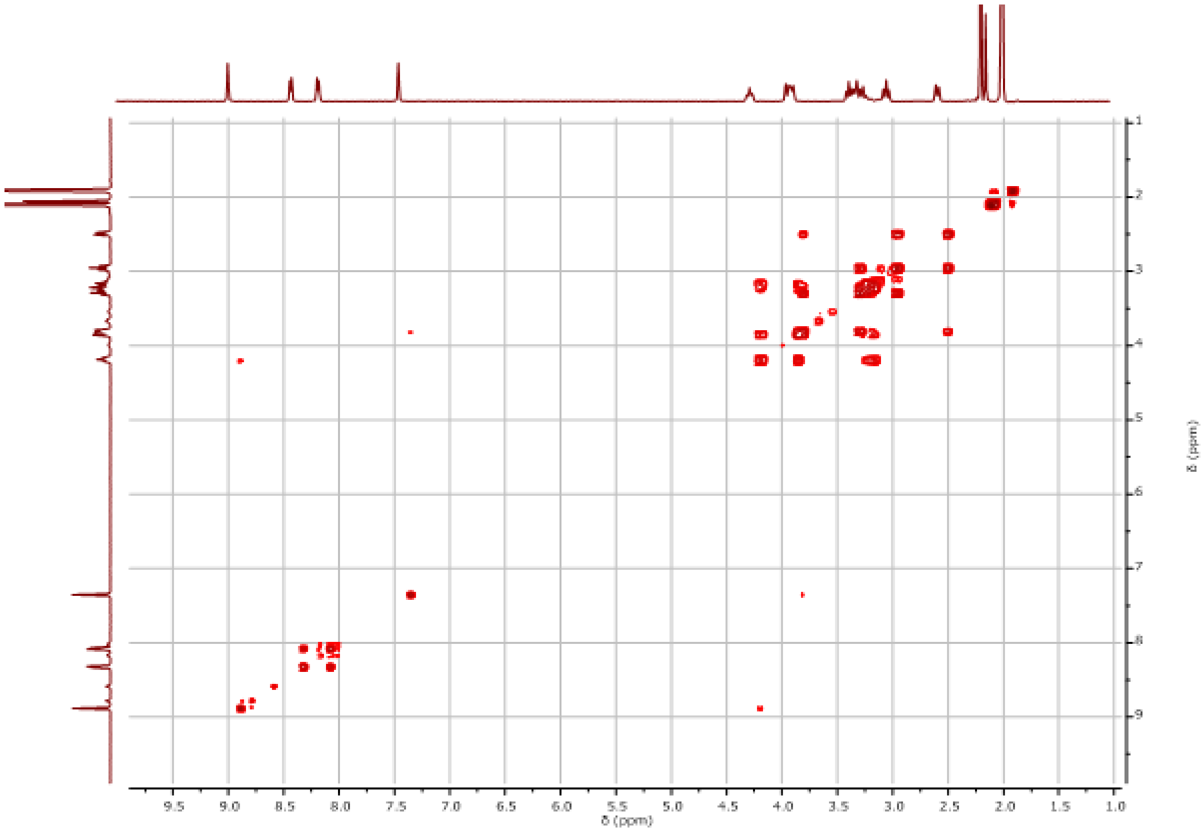

Figure S9. ^1H COSY NMR spectrum of $[\mathrm{Zn^{II}Cu^{I}}\mathbf{L}^{\mathrm{i}}](\mathrm{BF_4})_3$ (500 MHz, $CDCl_3$, 298 K).

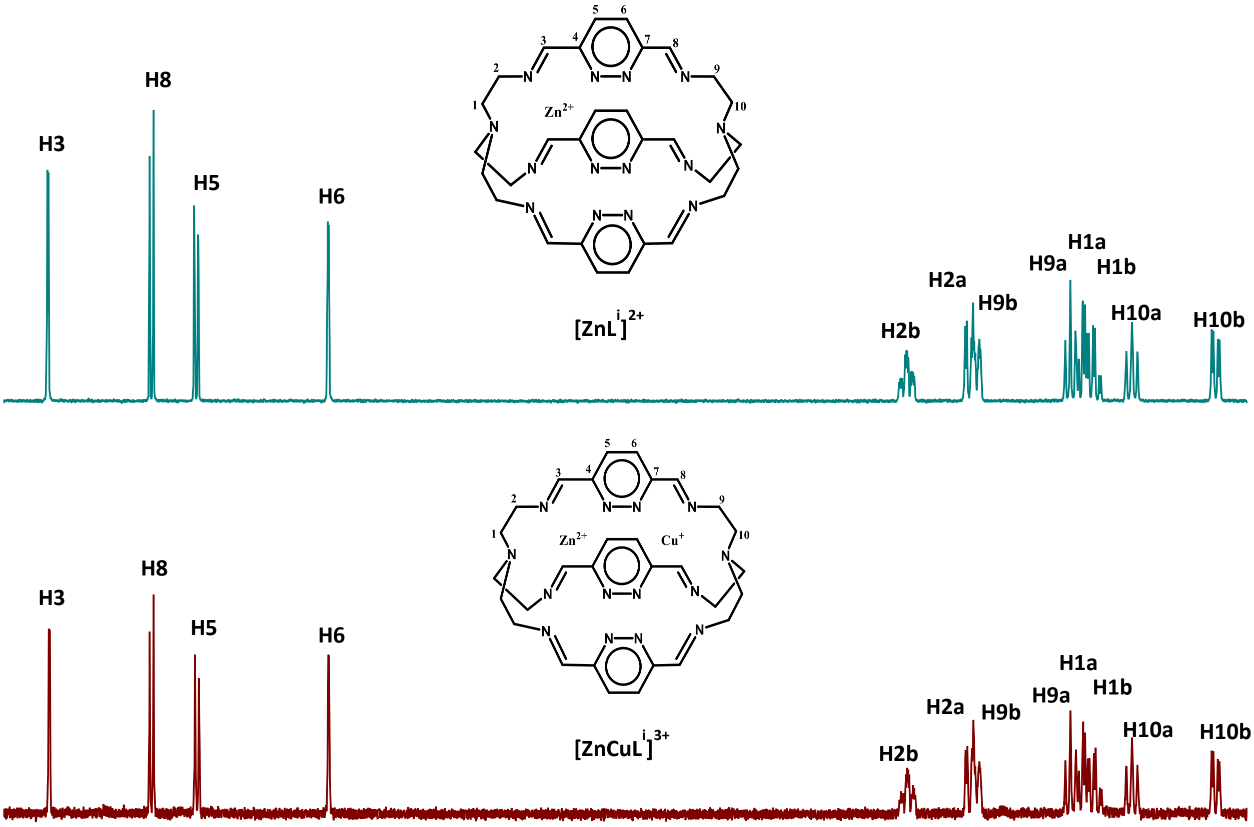

Figure S10. Stack plot of ^{1}H NMR spectrum of $[Zn^{II}\mathbf{L}^i](BF_4)_2.0.5H_2O$ (top) and $[Zn^{II}L^i](BF_4)_2$ (bottom) (400 MHz, CD_3CN, 298 K).

2 ESI-MS spectra of the cryptates

2.1 ESI-MS spectrum of the heterobimetallic cryptate, $[Zn^{II}Cu^{I}L^{i}](BF_4)_3$

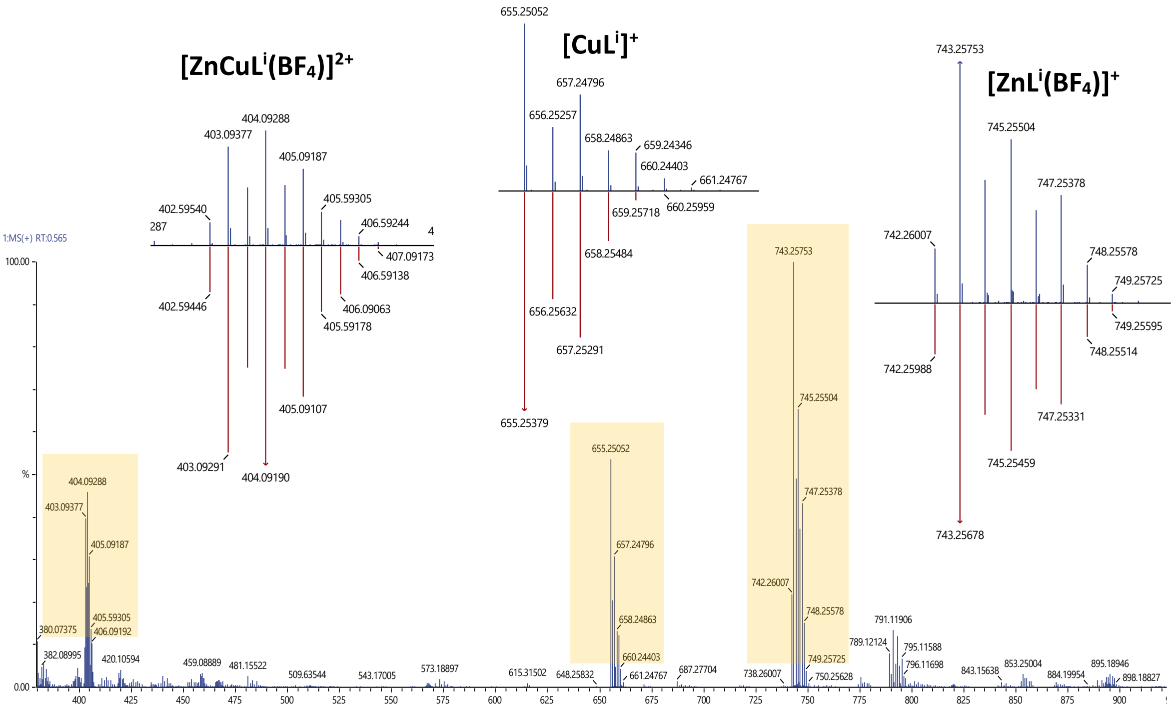

Figure S11. The ESI-MS of red needles (solvatomorph 1) of $[Zn^{II}Cu^{I}\mathbf{L}^{i}](BF_4)_3$. Inset: found (blue) and stimulated (red) spectrum for the peaks corresponding to the expansion and fit of the characteristic peaks.

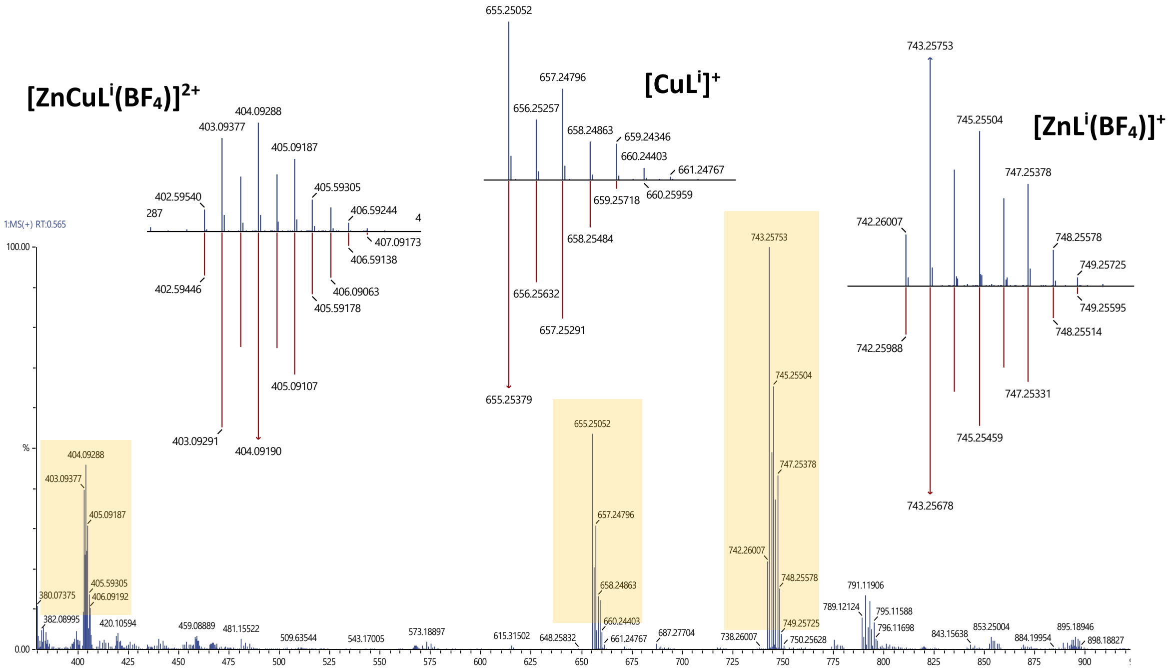

Figure S12. The ESI-MS of red blocks (solvatomorph 2) of [Zn^{II}Cu^{I}**L**^{i}](BF$_4$)$_3$. Inset: found (blue) and stimulated (red) spectrum for the peaks corresponding to the expansion and fit of the characteristic peaks.

2.2 ESI-MS spectrum of the mono-zinc cryptate, $[Zn^{II}L^{i}](BF_4)_2$

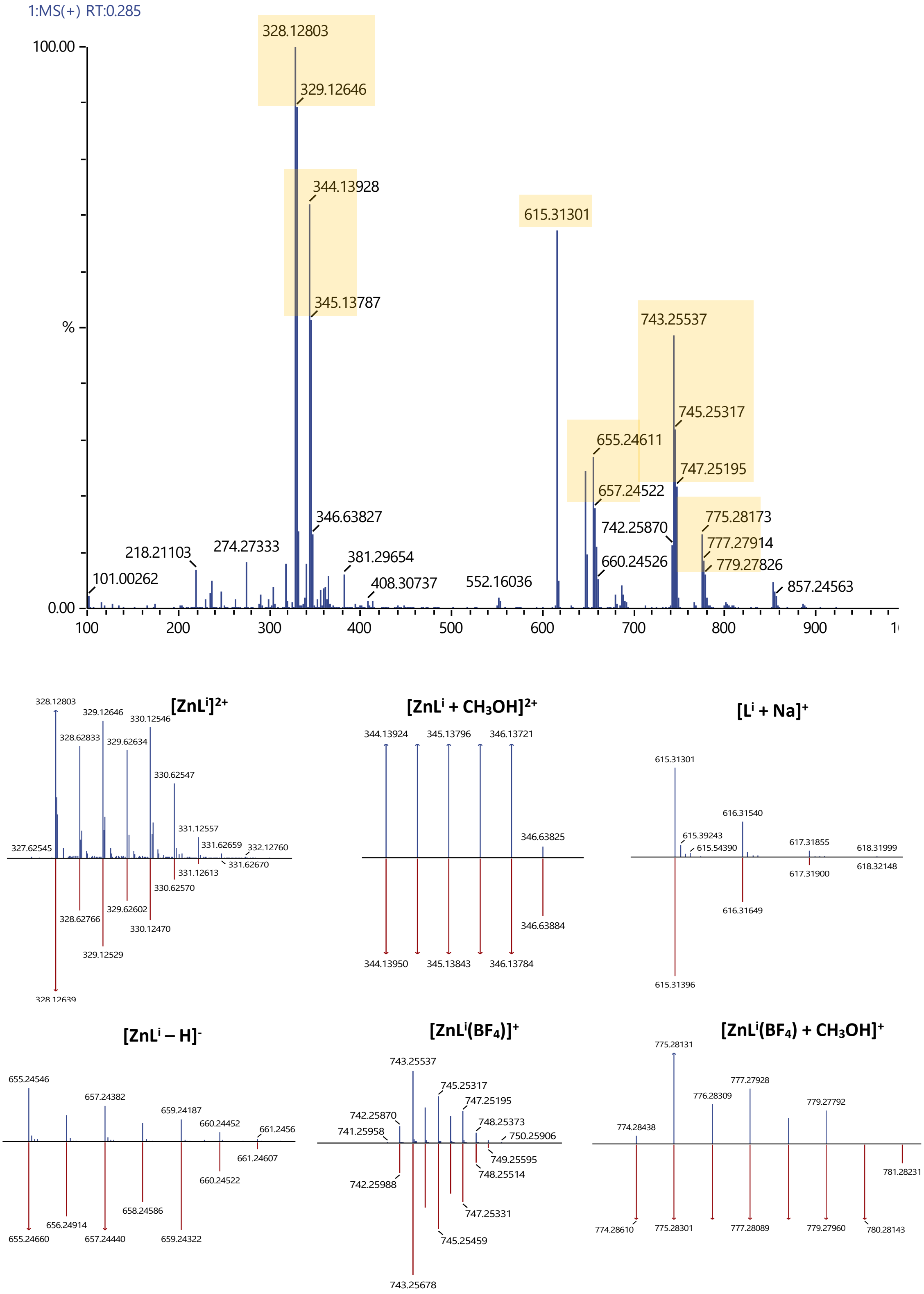

Figure S13. Top: The ESI-MS of $[Zn^{II}\mathbf{L}^{i}](BF_4)_2·0.5H_2O$ with peaks highlighted in yellow. Bottom: found (blue) and stimulated (red) spectrum for the peaks corresponding to the expansion and fit of the characteristic peaks.

3 X-ray crystallography on the new cryptates

X-ray crystallographic data were collected on an Oxford Diffraction SuperNova diffractometer with Atlas CCD, equipped with a Cryostream N_2 open-flow cooling device, using mirror monochromated micro-focus Cu-$K\alpha$ (1.54 Å) radiation at 100 K. A complete set of unique reflections to a maximum resolution of 0.82 Å was collected. Raw frame data (including data reduction, inter-frame scaling, unit cell refinement and absorption corrections) were processed using *CrysAlis Pro.*[1] The structure was solved and refined against all F^2 data using *SHELXL-2014.*[2] *OLEX2*[3] was used as the interface to visualise the structure during the refinement process. All non-H atoms were refined anisotropically unless otherwise stated. Hydrogen atoms were inserted at calculated positions with U(H) = 1.2 U (attached atom). High resolution pictures were prepared using Mercury[4] and POVray[5] software.

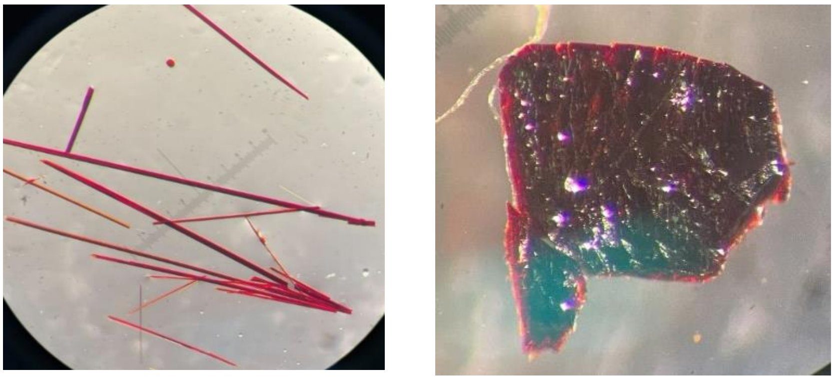

Figure S14. The two different crystals of $[\mathrm{Zn^{II}Cu^{I}}\mathbf{L}^{i}]^{3+}$, red needles (left, solvatomorph 1) and red blocks (right, solvatomorph 2) obtained by vapour diffusion of diethyl ether into a MeCN solution of this mixed metal cryptate.

3.1 X-ray crystallography of mixed metal cryptate, $[Zn^{II}Cu^{I}L^{i}](BF_4)_3$

3.1.1 X-ray crystallography of mixed metal cryptate – solvatomorph 1

Crystal data for red needles of $[Zn^{II}Cu^{I}L^{i}](BF_4)_3\cdot$ ½MeCN$\cdot$ ½H_2O (solvatomorph 1)

The two whole cryptates in the asymmetric unit were both ‘end-for-end’ disordered (Figure S17): in the first cryptate Zn01 and Cu02 are 0.85 occupancy (Zn1 and Cu2 minor occupancy, 0.15) and in the second cryptate, Zn04 and Cu3 are 0.55 occupancy (Zn03 and Cu1 minor occupancy, 0.45). Consequently, the pyridazine rings of all strands are also somewhat disordered and this too is modelled, with the partial occupancy C atoms kept isotropic; FLAT, ISOR, and EADP were used to restrain the atoms in the disordered pyridazine rings.

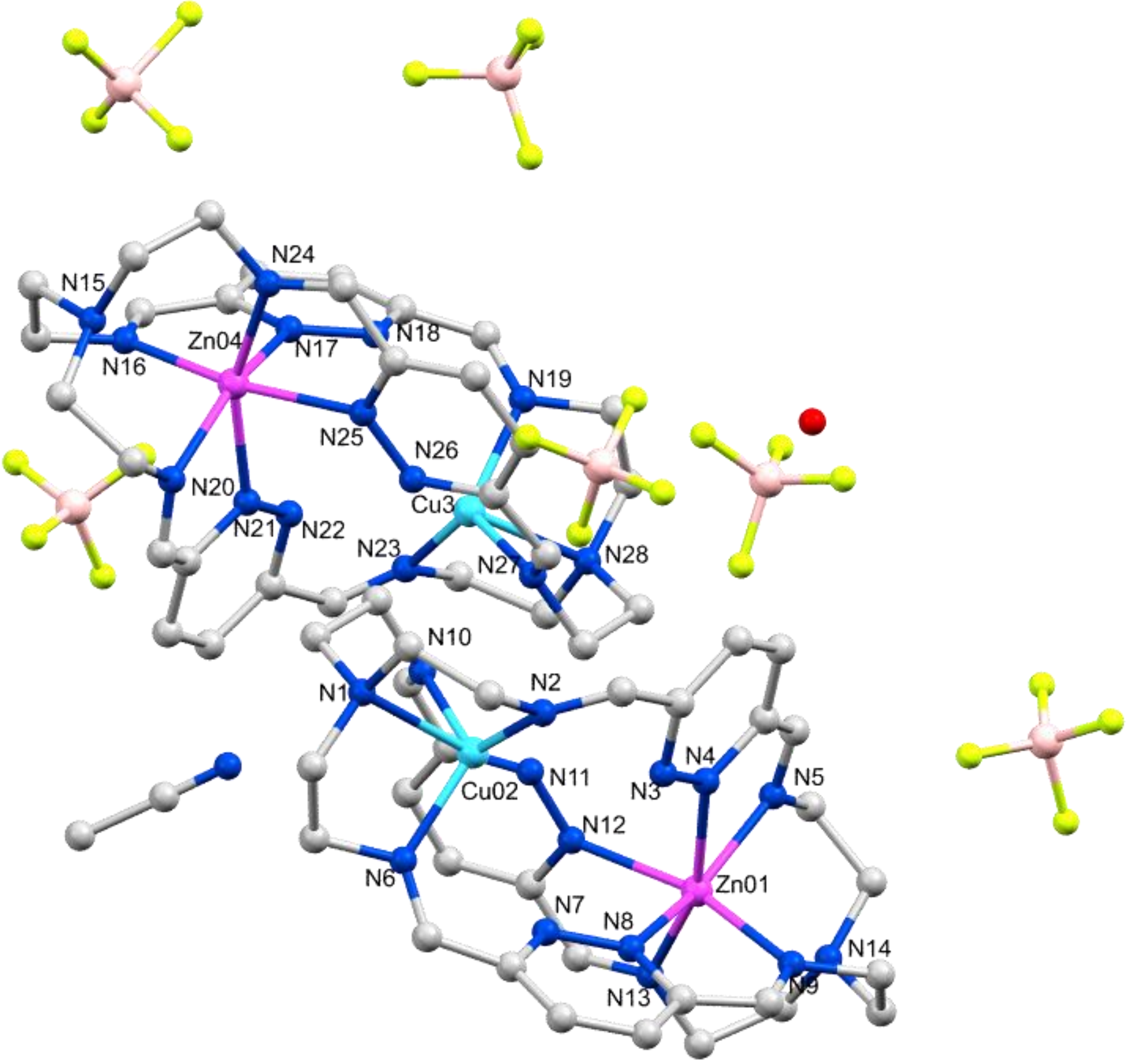

Figure S15. Perspective view of the asymmetric unit of the red needles of $[Zn^{II}Cu^{I}\mathbf{L}^{i}](BF_4)_3\cdot$½MeCN$\cdot$½$H_2O$ (solvatomorph 1) showing only the major occupancy form of the two independent cryptates, plus the 6 independent counter ions (BF_4), 1 MeCN and 1 H_2O in the asymmetric unit. For clarity, H atoms not shown.

Table S1 Crystal data and structure refinement details for the red needles, $[Zn^{II}Cu^{I}\mathbf{L}^{i}](BF_4)_3\cdot\frac{1}{2}MeCN\cdot\frac{1}{2}H_2O$ (solvatomorph 1)

	$([Zn^{II}Cu^{I}\mathbf{L}^{i}](BF_4)_3)_2\cdot H_2O\cdot CH_3CN$
Empirical formula	$C_{62}H_{77}B_6Cu_2F_{24}N_{29}OZn_2$ (two indpt dinuclear cryptates)
Formula weight	2023.20 (two indpt dinuclear cryptates, so halve this)
Temperature/K	100.00(10)
Crystal system	monoclinic
Space group	$P2_1/n$
a/Å	12.44760(10)
b/Å	26.5877(2)
c/Å	24.0965(2)
α/°	90
β/°	96.2500(10)
γ/°	90
Volume/Å^3	7927.41(11)
Z	4 (8 cryptates per unit cell)
ρ_{calc}g/cm^3	1.695
μ/mm^{-1}	2.354
F(000)	4096
Crystal size/mm^3	0.821 × 0.081 × 0.072
Radiation	Cu Kα (λ = 1.54184)
2θ range for data collection/°	7.382 to 145.768
Index ranges	$-15 \le h \le 13$, $-32 \le k \le 32$, $-29 \le l \le 29$
Reflections collected	73000
Independent reflections	15528 [R_{int} = 0.0636, R_{sigma} = 0.0348]
Data/restraints/parameters	15528/21/1209
Goodness-of-fit on F^2	1.147
Final R indexes [I>=2σ (I)]	R_1 = 0.0850, wR_2 = 0.1903
Final R indexes [all data]	R_1 = 0.0913, wR_2 = 0.1941
Largest diff. peak/hole / e Å^{-3}	0.89/-1.07

Table S2 Selected bond lengths [Å] and angles (°) for major occupancy form of red needles, $[Zn^{II}Cu^{I}\mathbf{L}^{i}](BF_4)_3$▪ ½MeCN▪ ½$H_2O$ (solvatomorph 1) for each of the two cryptates in the asymmetric unit.

Cryptate 1		**Cryptate 2**	
Bond Length [Å]		**Bond Length [Å]**	
Zn01-N5	2.110 (4)	Zn04-N24	2.127 (5)
Zn01-N9	2.138 (4)	Zn04-N17	2.138 (4)
Zn01-N13	2.150 (4)	Zn04-N25	2.147 (4)
Zn01-N8	2.165 (3)	Zn04-N16	2.152 (5)
Zn01-N12	2.187 (3)	Zn04-N20	2.156 (5)
Zn01-N4	2.263 (3)	Zn04-N21	2.175 (4)
Cu02-N2	1.988 (5)	Cu3-N27	1.970 (5)
Cu02-N6	2.021 (4)	Cu3-N23	1.998 (5)
Cu02-N10	2.032 (4)	Cu3-N19	2.017 (5)
Cu02-N1	2.321 (4)	Cu3-N8	2.380 (5)
Zn01-Cu02	5.098 (2)	Zn04-Cu3	4.969 (3)
Bond Angle [°]		**Bond Angle [°]**	
N5-Zn01-N9	101.63(17)	N16-Zn04-N20	99.56(18)
N5-Zn01-N13	107.99(17)	N16-Zn04-N21	93.8(2)
N5-Zn01-N12	97.58(15)	N24-Zn04-N16	107.53(18)
N5-Zn01-N8	153.67(17)	N24-Zn04-N20	105.48(18)
N5-Zn01-N4	73.65(14)	N24-Zn04-N21	157.9(2)
N9-Zn01-N13	104.86(17)	N24-Zn04-N25	75.28(17)
N9-Zn01-N12	159.94(16)	N24-Zn04-N17	97.0(2)
N9-Zn01-N8	74.24(14)	N20-Zn04-N21	75.48(18)
N9-Zn01-N4	92.50(16)	N25-Zn04-N16	161.8(2)
N13-Zn01-N12	74.19(15)	N25-Zn04-N20	96.8(2)
N13-Zn01-N8	98.10(15)	N25-Zn04-N21	82.7(2)
N13-Zn01-N4	161.58(16)	N17-Zn04-N16	76.15(19)
N12-Zn01-N4	87.40(12)	N17-Zn04-N20	157.3(2)
N8-Zn01-N12	85.98(12)	N17-Zn04-N21	82.5(2)
N8-Zn01-N4	80.49(12)	N17-Zn04-N25	85.7(2)
N6-Cu02-N10	114.74(18)	N27-Cu3-N23	122.8(2)
N6-Cu02-N1	81.78(15)	N27-Cu3-N19	116.0(2)
N10-Cu02-N1	80.12(16)	N27-Cu3-N28	80.17(17)
N2-Cu02-N6	115.66(18)	N23-Cu3-N19	112.1(2)
N2-Cu02-N10	122.99(18)	N23-Cu3-N28	80.48(17)
N2-Cu02-N1	82.32(17)	N19-Cu3-N28	78.85(17)

3.1.2 X-ray crystallography of mixed metal cryptate – solvatomorph 2

Crystal data for red blocks of [Zn^{II}Cu^{I}L^{i}](BF$_4$)$_3$·(solvatomorph 2)

No solvent of crystallisation in this solvatomorph. As for solvatomorph 1, the mixed metal cryptate in the asymmetric unit showed 'end-for-end' disorder (Figure S17): Zn1 and Cu1 are 0.80 occupancy (Zn2 and Cu2 minor occupancy, 0.20). Consequently, the pyridazine rings of all strands are also disordered and this too is modelled, with the partial occupancy C atoms kept isotropic; FLAT and ISOR were used to restrain the atoms in the disordered pyridazine rings.

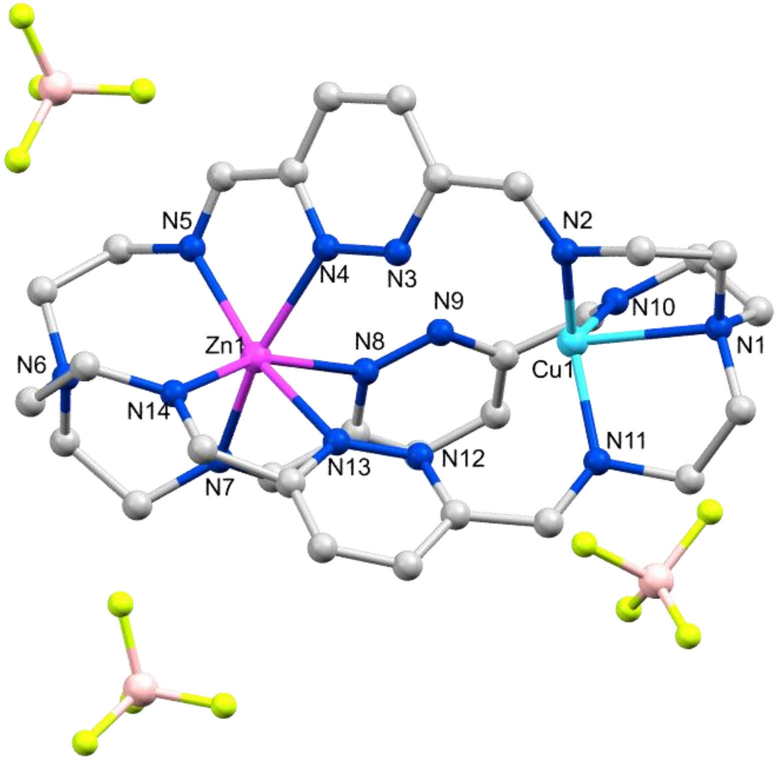

Figure S16. Perspective view of only the major occupancy form of the cryptate in the asymmetric unit for the red blocks of [Zn^{II}Cu^{I}**L**^{i}](BF$_4$)$_3$ (solvatomorph 2).

Table S3 Crystal data and structure refinement details for the red blocks, $[\mathrm{Zn^{II}Cu^{I}}\mathbf{L}^{\mathrm{i}}](\mathrm{BF_4})_3$ (solvatomorph 2).

	$[\mathrm{Zn^{II}Cu^{I}}\mathbf{L}^{\mathrm{i}}](\mathrm{BF_4})_3$
Empirical formula	$C_{30}H_{36}B_3CuF_{12}N_{14}Zn$
Formula weight	982.07
Temperature/K	100.01(10)
Crystal system	monoclinic
Space group	$P2_1/n$
a/Å	14.2639(4)
b/Å	14.9629(3)
c/Å	18.6926(6)
α/°	90
β/°	109.360(4)
γ/°	90
Volume/Å^3	3764.0(2)
Z	4
ρ_{calc}g/cm^3	1.733
μ/mm^{-1}	2.445
F(000)	1984
Crystal size/mm^3	0.26 × 0.226 × 0.16
Radiation	Cu Kα (λ = 1.54184)
2Θ range for data collection/°	7.748 to 145.298
Index ranges	$-17 \le h \le 17$, $-17 \le k \le 18$, $-23 \le l \le 22$
Reflections collected	34554
Independent reflections	7378 [R_{int} = 0.0422, R_{sigma} = 0.0326]
Data/restraints/parameters	7378/19/663
Goodness-of-fit on F^2	1.136
Final R indexes [I>=2σ (I)]	R_1 = 0.0601, wR_2 = 0.1421
Final R indexes [all data]	R_1 = 0.0789, wR_2 = 0.1513
Largest diff. peak/hole / e Å^{-3}	1.19/-0.48

Table S4 Selected bond lengths [Å] and angles (°) for the major occupancy form of the cryptate in the red needles of $[\mathrm{Zn^{II}Cu^{I}}\mathbf{L}^{\mathrm{i}}](\mathrm{BF_4})_3$ (solvatomorph 2).

Bond Length [Å]	
Zn1-N5	2.117 (3)
Zn1-N7	2.160 (4)
Zn1-N14	2.204 (4)
Zn1-N8	2.205 (4)
Zn1-N4	2.219 (4)
Zn1-N13	2.280 (4)
Cu1-N2	1.988 (4)
Cu1-N11	1.990 (4)
Cu1-N10	2.001 (4)
Cu1-N1	2.355 (3)
Zn1-Cu1	5.115 (14)

Bond Angle [°]	
N5-Zn1-N14	101.25(13)
N5-Zn1-N7	105.21(14)
N5-Zn1-N4	74.94(14)
N5-Zn1-N8	103.66(14)
N5-Zn1-N13	159.87(16)
N14-Zn1-N4	100.94(16)
N14-Zn1-N13	73.54(14)
N7-Zn1-N14	97.32(14)
N7-Zn1-N4	161.35(16)
N7-Zn1-N8	75.51(15)
N7-Zn1-N13	94.81(15)
N4-Zn1-N13	86.82(16)
N8-Zn1-N14	155.09(14)
N8-Zn1-N4	86.27(17)
N8-Zn1-N13	83.20(15)
N11-Cu1-N10	117.30(15)
N11-Cu1-N1	81.14(13)
N10-Cu1-N1	80.99(14)
N2-Cu1-N11	120.49(16)
N2-Cu1-N10	114.85(15)
N2-Cu1-N1	80.58(13)

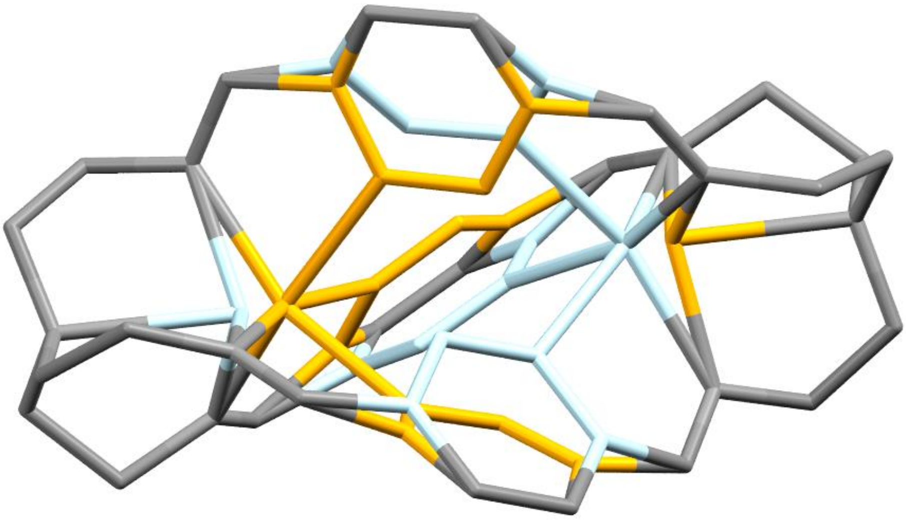

Figure S17. The “end-for-end” disorder, major occupancy (orange) and minor occupancy (light blue), observed in both crystal structures of [Zn^{II}Cu^{I}**L**^{i}]$^{3+}$.

3.2 X-ray crystallography of mono-zinc cryptate, [Zn^{II}L^{i}](BF$_4$)$_2$

Figure S18. The clear pale blocks of [Zn^{II}**L**^{i}]$^{2+}$, obtained by vapour diffusion of diethyl ether into a MeCN solution of cryptate.

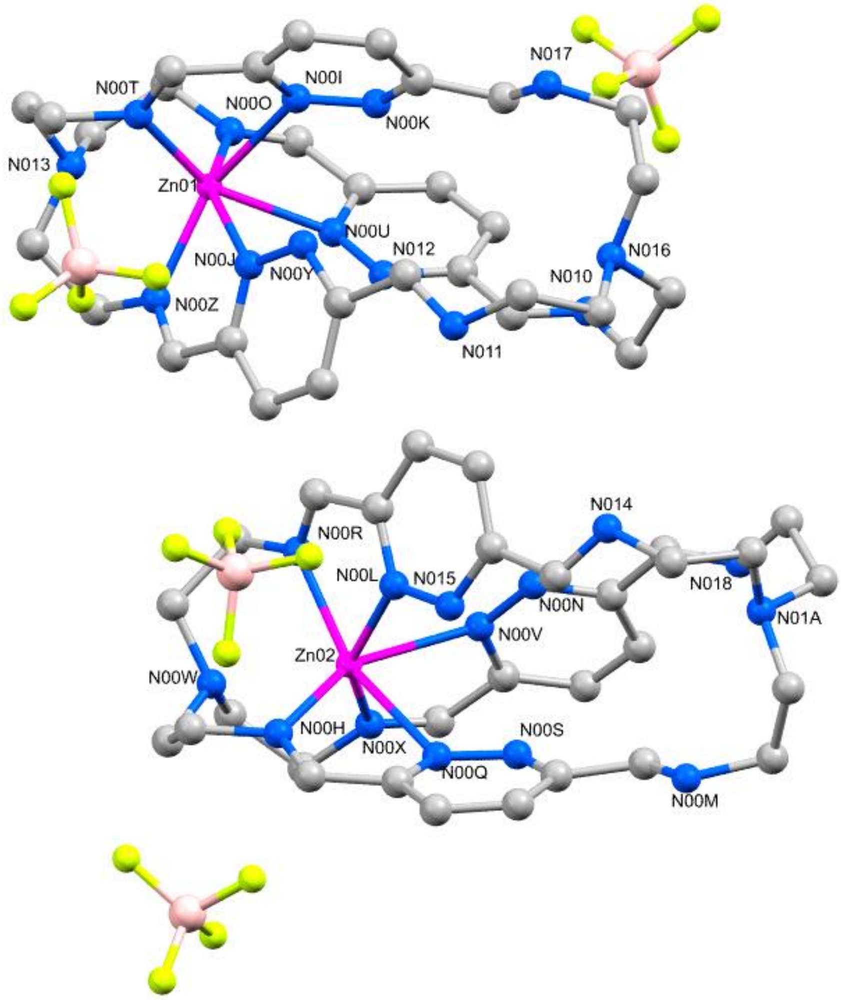

Figure S19. Perspective view of the asymmetric unit of $[\mathrm{Zn^{II}}\mathbf{L}^{\mathbf{i}}](\mathrm{BF_4})_2$, containing two cryptates and four counter ions.

Table S5 Crystal data and structure refinement details for $[\mathrm{Zn}^{II}\mathbf{L}^{i}](\mathrm{BF}_4)_2$

	$[\mathrm{Zn}^{II}\mathbf{L}^{i}](\mathrm{BF}_4)_2$
Empirical formula	$C_{30}H_{36}B_2F_8N_{14}Zn$
Formula weight	831.72
Temperature/K	100.01(10)
Crystal system	triclinic
Space group	P-1
a/Å	9.5340(2)
b/Å	13.1923(4)
c/Å	28.9592(6)
α/°	85.359(2)
β/°	87.624(2)
γ/°	76.780(2)
Volume/Å^3	3533.21(15)
Z	4
ρ_{calc}g/cm^3	1.564
μ/mm^{-1}	1.755
F(000)	1704
Crystal size/mm^3	0.231 × 0.201 × 0.177
Radiation	Cu Kα (λ = 1.54184)
2θ range for data collection/°	6.902 to 145.844
Index ranges	$-11 \le h \le 11, -16 \le k \le 16, -33 \le l \le 35$
Reflections collected	52456
Independent reflections	13811 [$R_{int} = 0.0279$, $R_{sigma} = 0.0218$]
Data/restraints/parameters	13811/0/992
Goodness-of-fit on F^2	1.207
Final R indexes [I>=2σ (I)]	$R_1 = 0.0611$, $wR_2 = 0.1526$
Final R indexes [all data]	$R_1 = 0.0650$, $wR_2 = 0.1544$
Largest diff. peak/hole / e Å^{-3}	0.82/-0.50

Crystal data for $[\mathrm{Zn}^{II}\mathrm{L}^{i}](\mathrm{BF}_4)_2$

PLATON indicated the presence of twinning so the suggested TWIN -1 0 0 0 -1 0 0 0 1 and BASF 0.09 commands were used to model this.

Table S6 Selected bond lengths [Å] and angles (°) for two of the $[\mathrm{Zn^{II}}\mathbf{L^{i}}](\mathrm{BF_4})_2$ (Cryptate A and B) in the asymmetric unit.

Cryptate A		**Cryptate B**	
Bond Length [Å]		**Bond Length [Å]**	
Zn01-N00T	2.089 (4)	Zn02-N00X	2.085 (4)
Zn01-N00O	2.095 (4)	Zn02-N00H	2.087 (4)
Zn01-N00Z	2.100 (4)	Zn02-N00R	2.106 (4)
Zn01-N00J	2.303 (4)	Zn02-N00L	2.295 (4)
Zn01-N00Y	2.322 (4)	Zn02-N00V	2.389 (4)
Zn01-N00I	2.362 (4)	Zn02-N00Q	2.441 (4)
Bond Angle [°]		**Bond Angle [°]**	
N00J-Zn01-N00I	78.71(12)	N00H-Zn02-N00L	92.56(13)
N00J-Zn01-N00U	78.61(12)	N00H-Zn02-N00Q	72.03(13)
N00O-Zn01-N00I	93.02(12)	N00H-Zn02-N00R	111.22(14)
N00O-Zn01-N00J	151.99(13)	N00H-Zn02-N00V	148.79(13)
N00O-Zn01-N00U	73.54(13)	N00L-Zn02-N00Q	78.27(12)
N00O-Zn01-N00Z	109.56(13)	N00L-Zn02-N00V	77.60(12)
N00T-Zn01-N00I	72.87(13)	N00R-Zn02-N00L	74.38(13)
N00T-Zn01-N00J	92.07(13)	N00R-Zn02-N00Q	152.55(13)
N00T-Zn01-N00O	111.20(14)	N00R-Zn02-N00V	94.75(13)
N00T-Zn01-N00U	151.78(13)	N00V-Zn02-N00Q	76.96(12)
N00T-Zn01-N00Z	110.88(14)	N00X-Zn02-N00H	111.02(14)
N00U-Zn01-N00I	79.17(12)	N00X-Zn02-N00L	150.00(13)
N00Z-Zn01-N00I	152.64(13)	N00X-Zn02-N00Q	91.26(13)
N00Z-Zn01-N00J	74.12(13)	N00X-Zn02-N00R	111.45(14)
N00Z-Zn01-N00U	92.29(13)	N00X-Zn02-N00V	72.64(13)

4 Electrochemistry and electrocatalytic HER

4.1 General electrochemistry details

General method: All electrochemical measurements were carried out in a three neck H-shaped electrochemical (Figure S19) cell under an argon atmosphere (all solutions were purged with Ar for 20-30 min prior to study), using an IVIUMSATT.XRE potentiostat, a glassy carbon (3 mm diameter, surface area = 0.071 cm^2) as the working electrode, 0.01 M $AgNO_3$/Ag as the reference electrode, platinum sheet as the counter electrode. The working electrode compartment was filled with 8 mL of 0.1 M Bu_4NPF_6 acetonitrile solution, and the rest of the "H" was filled with ca. 10 mL of 0.1 M Bu_4NPF_6 acetonitrile solution. Ferrocene was used as an internal reference check.

Acetonitrile was freshly distilled over calcium hydride. Bu_4NPF_6 (99 %, for electrochemical analysis) was purchased from Sigma Aldrich and used without further purification.

The working electrode was cleaned before each measurement by: rinsing with water and acetone, then polishing with alumina slurry, and finally rinsing with acetone and drying.

The three neck H-shaped electrochemical cell and Pt counter electrode were carefully cleaned and dried between studies as follows: filled and soaked in hydrochloric acid (1 hour), rinsed thoroughly with copious water, filled and soaked in water (2 hours), rinsed with water, acetonitrile and acetone, soaked in dry MeCN for 24 hours, emptied and dried in an oven overnight before use.

Cyclic Voltammetry (CV): CVs where carried out on 1 mM, 8 mL acetonitrile solutions of cryptates or the salt $Cu^I(MeCN)_4(BF_4)$, and 0.1 M Bu_4NPF_6 electrolyte. An internal reference check to the ferrocene/ferrocenium cation couple ($Fc^{+/0}$) was carried out at the conclusion of every study, and was consistently observed at $E_{1/2} = 0.09 \pm 0.01$ V, with $\Delta E = 0.09$ V, vs 0.01 M $AgNO_3$/Ag. Prior to each study, the purity of the electrolyte and solvent and the cleanliness of the cell setup was first checked by recording the CV from 0 to 2.0 to -2.0 to 0 V to confirm negligible background current was observed, before adding the respective copper complex and commencing the study.

Controlled Potential Electrolysis (CPE): CPE measurements were conducted using same cell described above, but in this case the working compartment was filled with 8 mL of 0.1 M Bu_4NPF_6 acetonitrile solution containing the specified amount of acid (0.08 M unless otherwise stated) and 1 mM in the copper complex. The remainder of the 'H' was filled with ca. 10 mL of 0.1 M Bu_4NPF_6 acetonitrile solution. Glassy carbon electrode (0.071 cm^2) and the 0.01 M $AgNO_3$/Ag reference electrode were placed into the working compartment, and the Pt sheet counter electrode was placed in the auxiliary compartment. The reported, very modest, TON values were calculated assuming that the Faradaic efficiency (FE) is 100%. - the observed activity was insufficient to warrant additional, offsite, electrochemical studies with a gas chromatograph attached to quantify the hydrogen evolved and determine the FE.

Additional reference electrode checks: The check was done by taking the reference electrode out, rinsing it and placing it into a separate electrochemical cell containing 1 mM ferrocene in the same electrolyte solution and running the CV. These checks on the reference electrode, before and after CVs and CPE experiments on cryptates with acid present, showed that no drift was observed during these experiments, as $E_{1/2}(Fc^+/Fc) = 0.09 \pm 0.01$ V vs 0.01 M $AgNO_3$/Ag, with $\Delta E = 0.09 \pm 0.01$ V, in all cases (Figure S21).

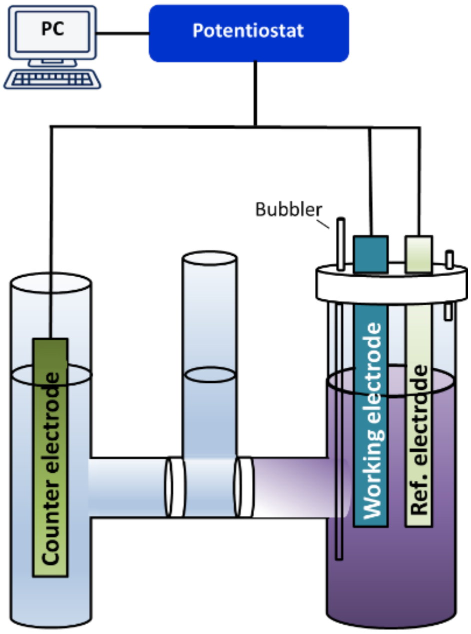

Figure S20. Schematic representation of the electrochemical H-cell used for experiments.

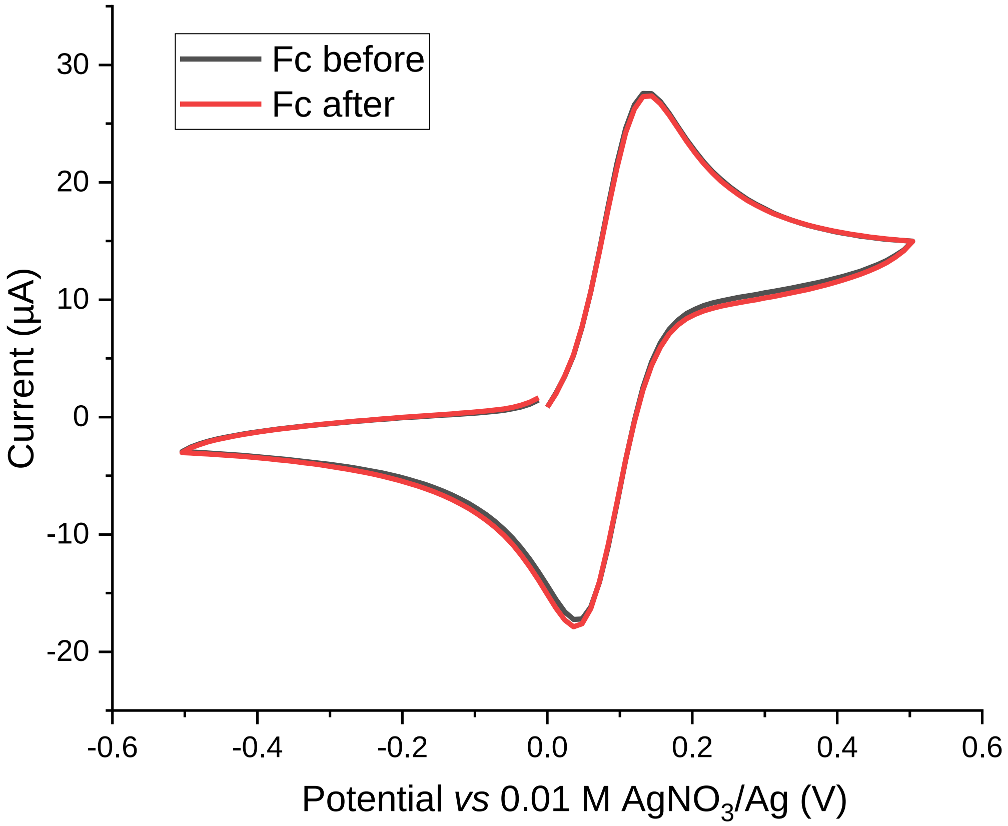

Figure S21. Exemplar of the before and after reference checks showing there is no drift before and after collecting CVs and CPE experiments: $E_{1/2}(Fc^+/Fc)$ = 0.09 ± 0.01 V vs 0.01 M $AgNO_3/Ag$, with ΔE = 0.09 ± 0.01 V. Conditions: 0.1 M $(Bu_4N)PF_6$, 3 mm glassy carbon working (A = 0.071 cm^2) and Pt counter electrode, 100 mV/s.

4.2 Cyclic voltammetry of cryptates; scan rate studies

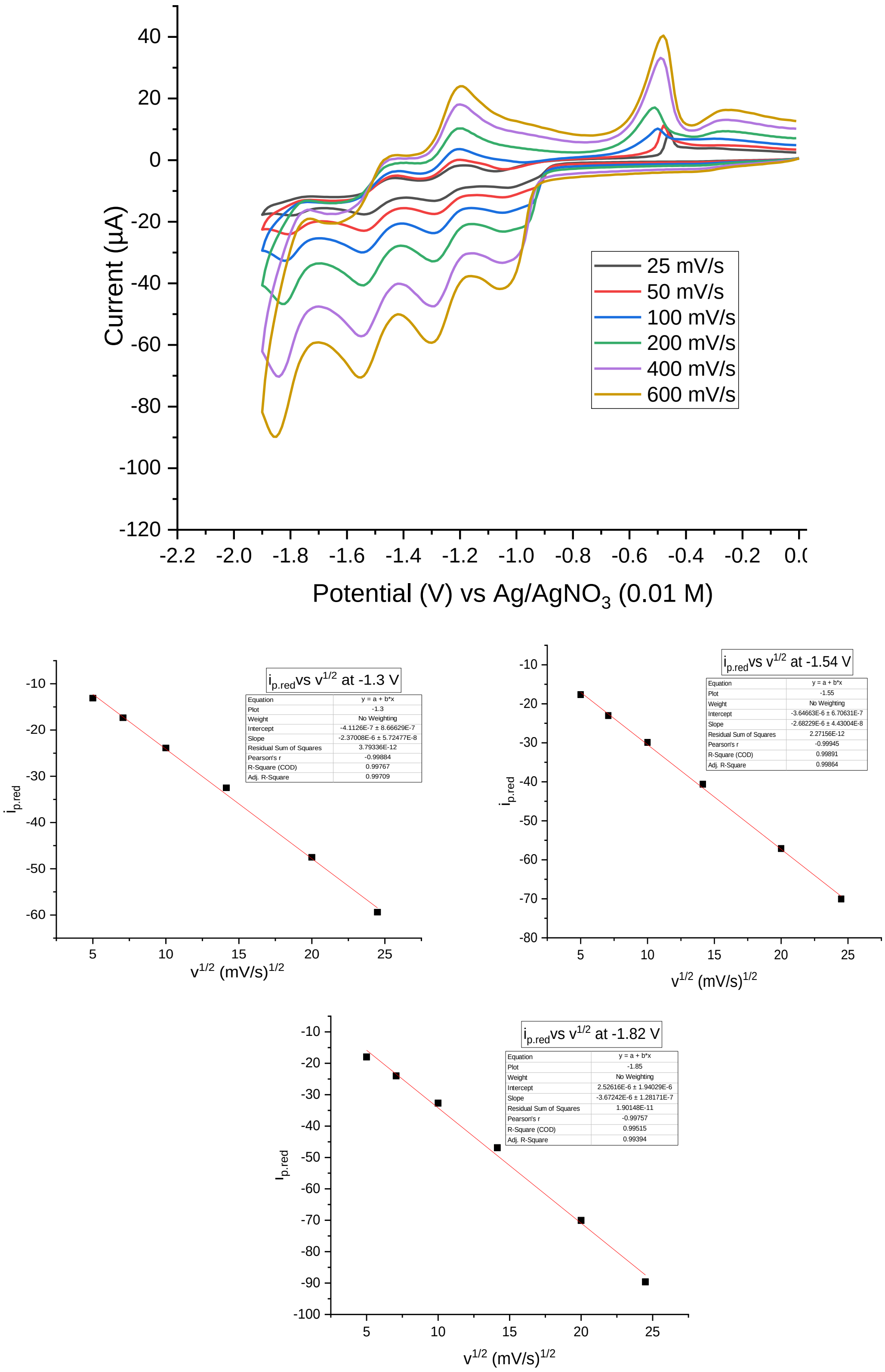

Equation	y = a + b*x
Plot	-1.3
Weight	No Weighting
Intercept	-4.1126E-7 ± 8.66629E-7
Slope	-2.37008E-6 ± 5.72477E-8
Residual Sum of Squares	3.79336E-12
Pearson's r	-0.99884
R-Square (COD)	0.99767
Adj. R-Square	0.99709

Equation	y = a + b*x
Plot	-1.55
Weight	No Weighting
Intercept	-3.64663E-6 ± 6.70631E-7
Slope	-2.68229E-6 ± 4.43004E-8
Residual Sum of Squares	2.27156E-12
Pearson's r	-0.99945
R-Square (COD)	0.99891
Adj. R-Square	0.99864

Equation	y = a + b*x
Plot	-1.85
Weight	No Weighting
Intercept	2.52616E-6 ± 1.94029E-6
Slope	-3.67242E-6 ± 1.28171E-7
Residual Sum of Squares	1.90148E-11
Pearson's r	-0.99757
R-Square (COD)	0.99515
Adj. R-Square	0.99394

Figure S22. CV's from 0→-1.9→0 V, at varying scan rates, for 1 mM MeCN solution of $[Zn^{II}Cu^{I}\mathbf{L}^{i}]^{3+}$, and plots of cathodic peak current versus the square root of the scan rate ($\boldsymbol{\upsilon^{1/2}}$) for the 3 redox events at E_{pc} = -1.29 V (diffusion coefficient (*D*) = 1.52 × 10^{-8} $cm^2\,s^{-1}$), E_{pc} = -1.54 V (*D* = 1.94 × 10^{-8} $cm^2\,s^{-1}$), and E_{pc} = -1.84 V (*D* = 3.64 ×10^{-8} $cm^2\,s^{-1}$).

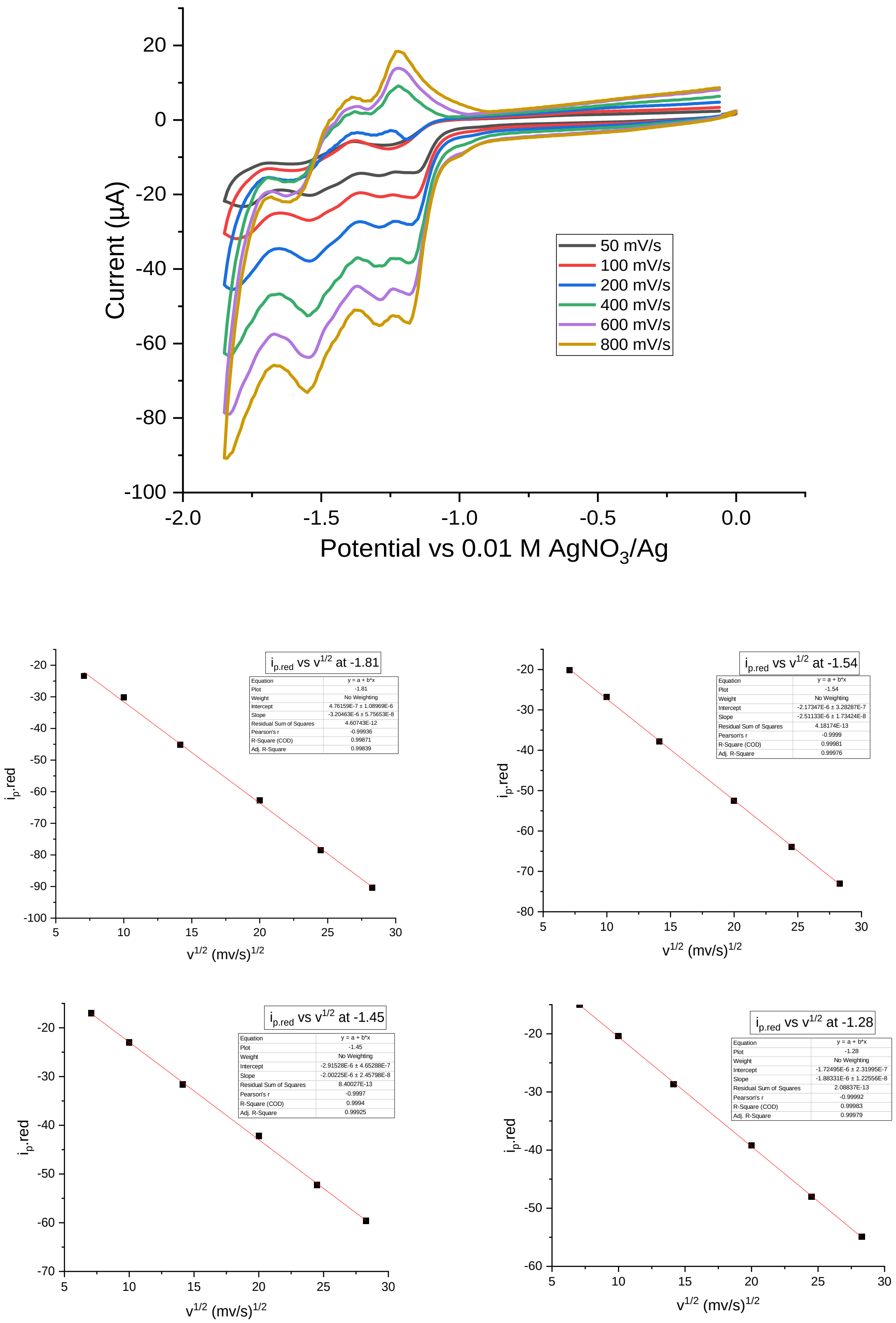

Equation	y = a + b*x
Plot	-1.81
Weight	No Weighting
Intercept	4.76159E-7 ± 1.08969E-6
Slope	-3.20463E-6 ± 5.75653E-8
Residual Sum of Squares	4.60743E-12
Pearson's r	-0.99936
R-Square (COD)	0.99871
Adj. R-Square	0.99839

Equation	y = a + b*x
Plot	-1.54
Weight	No Weighting
Intercept	-2.17347E-6 ± 3.28287E-7
Slope	-2.51133E-6 ± 1.73424E-8
Residual Sum of Squares	4.18174E-13
Pearson's r	-0.9999
R-Square (COD)	0.99981
Adj. R-Square	0.99976

Equation	y = a + b*x
Plot	-1.45
Weight	No Weighting
Intercept	-2.91528E-6 ± 4.65288E-7
Slope	-2.00225E-6 ± 2.45798E-8
Residual Sum of Squares	8.40027E-13
Pearson's r	-0.9997
R-Square (COD)	0.9994
Adj. R-Square	0.99925

Equation	y = a + b*x
Plot	-1.28
Weight	No Weighting
Intercept	-1.72495E-6 ± 2.31995E-7
Slope	-1.88331E-6 ± 1.22556E-8
Residual Sum of Squares	2.08837E-13
Pearson's r	-0.99992
R-Square (COD)	0.99983
Adj. R-Square	0.99979

Figure S23. CV's from 0→-1.9→0 V, at varying scan rates, for 1 mM MeCN solution of $[\mathrm{Zn^{II}}\mathbf{L}^{i}]^{2+}$, and and plots of cathodic peak current versus the square root of the scan rate ($\boldsymbol{\upsilon}^{1/2}$) for the 4 redox events at E_{pc} = -1.28 V (Diffusion coefficient, (*D*) = 9.04×10^{-9} cm^2 s^{-1}), E_{pc} = -1.45 V (*D* = 1.08×10^{-8} cm^2 s^{-1}), E_{pc} = -1.54 V (*D* = 1.69×10^{-8} cm^2 s^{-1}), and E_{pc} = -1.82 V (*D* = 2.76×10^{-8} cm^2 s^{-1}).

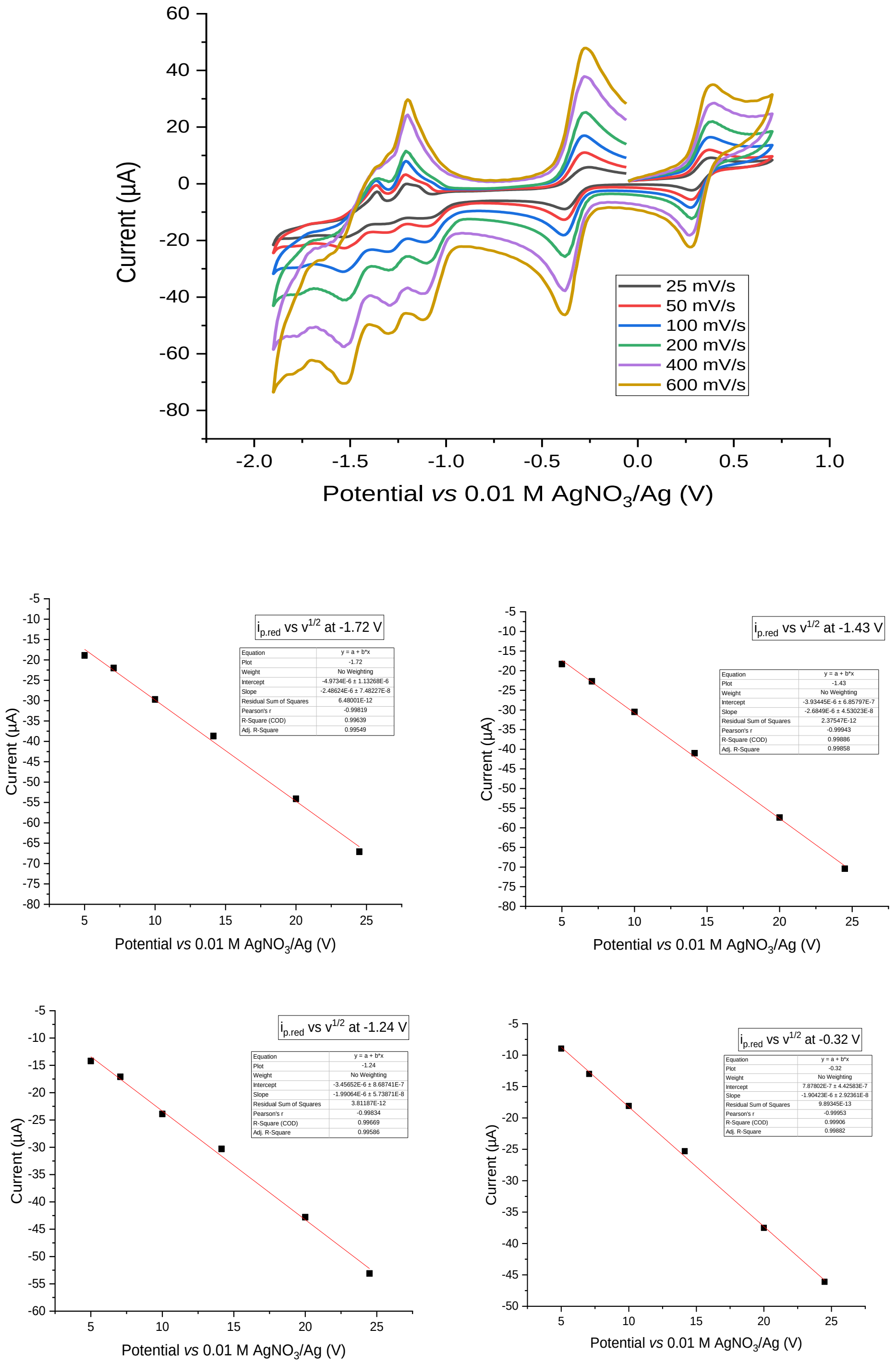

Equation	y = a + b*x
Plot	-1.72
Weight	No Weighting
Intercept	-4.9734E-6 ± 1.13268E-6
Slope	-2.48624E-6 ± 7.48227E-8
Residual Sum of Squares	6.48001E-12
Pearson's r	-0.99819
R-Square (COD)	0.99639
Adj. R-Square	0.99549

Equation	y = a + b*x
Plot	-1.43
Weight	No Weighting
Intercept	-3.93445E-6 ± 6.85797E-7
Slope	-2.6849E-6 ± 4.53023E-8
Residual Sum of Squares	2.37547E-12
Pearson's r	-0.99943
R-Square (COD)	0.99886
Adj. R-Square	0.99858

Equation	y = a + b*x
Plot	-1.24
Weight	No Weighting
Intercept	-3.45652E-6 ± 8.68741E-7
Slope	-1.99064E-6 ± 5.73871E-8
Residual Sum of Squares	3.81187E-12
Pearson's r	-0.99834
R-Square (COD)	0.99669
Adj. R-Square	0.99586

Equation	y = a + b*x
Plot	-0.32
Weight	No Weighting
Intercept	7.87802E-7 ± 4.42583E-7
Slope	-1.90423E-6 ± 2.92361E-8
Residual Sum of Squares	9.89345E-13
Pearson's r	-0.99953
R-Square (COD)	0.99906
Adj. R-Square	0.99882

Figure S24. CV's from 0→0.7→-1.9→0 V, at varying scan rates, for 1 mM MeCN solution of $[\mathrm{Cu^{II}Cu^{I}}\mathbf{L}]^{3+}$, and and plots of cathodic peak current versus the square root of the scan rate ($\boldsymbol{v}^{1/2}$) for the 4 redox events at E_{pc} = -0.34 V (Diffusion coefficient, (D) = 9.75 × 10^{-9} cm^2 s^{-1}), E_{pc} = -1.29 V (D = 1.07 × 10^{-8} cm^2 s^{-1}), E_{pc} = -1.52 V (D = 1.94 × $10^{-8}$$cm^2$ s^{-1}), and E_{pc} = -1.77 V (D = 1.67 × $10^{-8}$$cm^2$ s^{-1}).

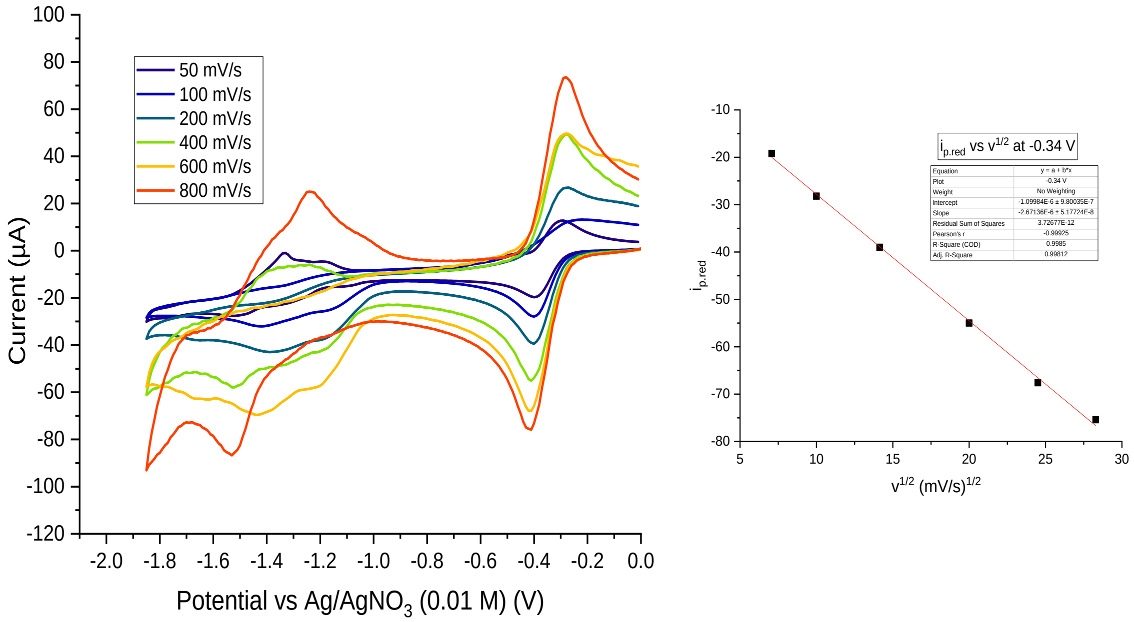

Figure S25. CV's from 0→-1.9→0 V, at varying scan rates, for 1 mM MeCN solution of $[Cu^{II}\mathbf{L}^{i}]^{2+}$ and and plots of cathodic peak current versus the square root of the scan rate ($\boldsymbol{v}^{1/2}$) for the redox event at E_{pc} = -0.40 V (Diffusion coefficient, (*D*) = 1.92×10^{-8} $cm^2\ s^{-1}$).

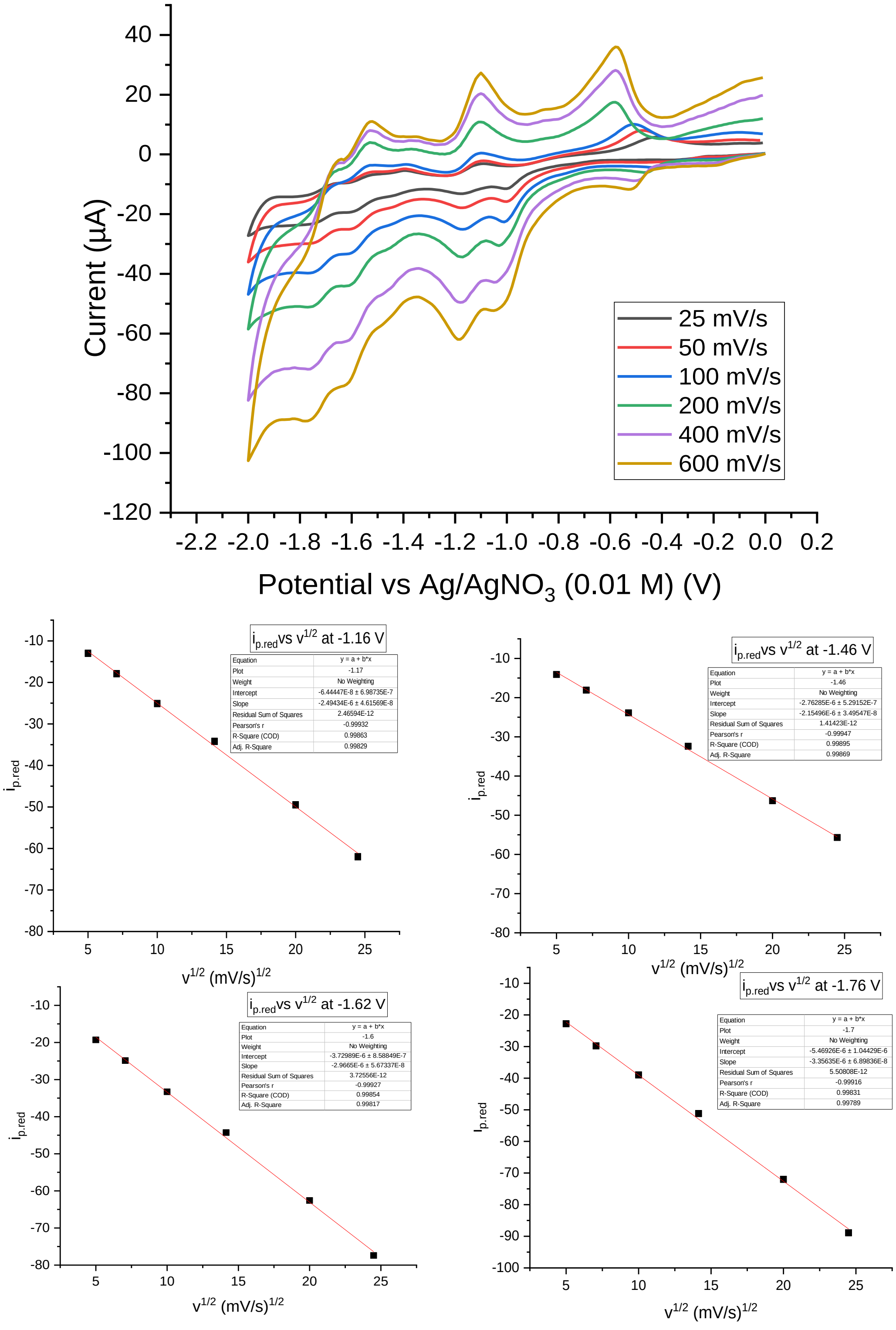

Equation	y = a + b*x
Plot	-1.17
Weight	No Weighting
Intercept	-6.44447E-8 ± 6.98735E-7
Slope	-2.49434E-6 ± 4.61569E-8
Residual Sum of Squares	2.46594E-12
Pearson's r	-0.99932
R-Square (COD)	0.99863
Adj. R-Square	0.99829

Equation	y = a + b*x
Plot	-1.46
Weight	No Weighting
Intercept	-2.76285E-6 ± 5.29152E-7
Slope	-2.15496E-6 ± 3.49547E-8
Residual Sum of Squares	1.41423E-12
Pearson's r	-0.99947
R-Square (COD)	0.99895
Adj. R-Square	0.99869

Equation	y = a + b*x
Plot	-1.6
Weight	No Weighting
Intercept	-3.72989E-6 ± 8.58849E-7
Slope	-2.9665E-6 ± 5.67337E-8
Residual Sum of Squares	3.72556E-12
Pearson's r	-0.99927
R-Square (COD)	0.99854
Adj. R-Square	0.99817

Equation	y = a + b*x
Plot	-1.7
Weight	No Weighting
Intercept	-5.46926E-6 ± 1.04429E-6
Slope	-3.35635E-6 ± 6.89836E-8
Residual Sum of Squares	5.50808E-12
Pearson's r	-0.99916
R-Square (COD)	0.99831
Adj. R-Square	0.99789

Figure S26. CV's from 0→-1.9→0 V, at varying scan rates, for 1 mM MeCN solution of $[\mathrm{Co^{II}Cu^{I}}\mathbf{L}^{\mathrm{i}}]^{3+}$, and and plots of cathodic peak current versus the square root of the scan rate ($\boldsymbol{v}^{1/2}$) for the 4 redox events at E_{pc} = -1.11 V (Diffusion coefficient, (*D*) = 1.67 × 10^{-8} cm^2 s^{-1}), E_{pc} = -1.46 V (*D* = 1.25 × 10^{-8} cm^2 s^{-1}), E_{pc} = -1.59 V (*D* = 2.37 × 10^{-8} cm^2 s^{-1}), and E_{pc} = -1.76 V (*D* = 3.03 × 10^{-8} cm^2 s^{-1}).

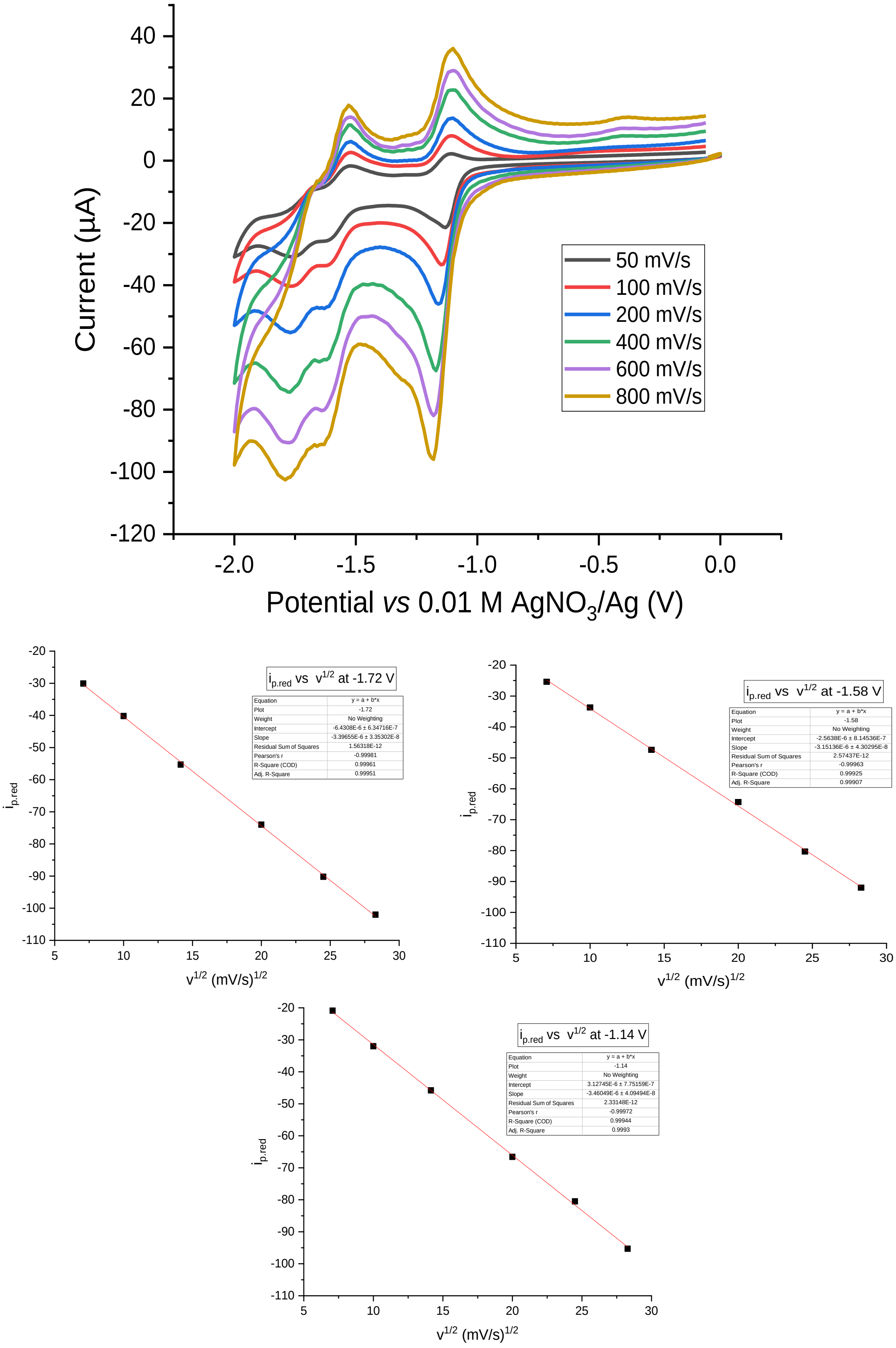

Equation	y = a + b*x
Plot	-1.72
Weight	No Weighting
Intercept	-6.4308E-6 ± 6.34716E-7
Slope	-3.39655E-6 ± 3.35302E-8
Residual Sum of Squares	1.56318E-12
Pearson's r	-0.99981
R-Square (COD)	0.99961
Adj. R-Square	0.99951

Equation	y = a + b*x
Plot	-1.58
Weight	No Weighting
Intercept	-2.5638E-6 ± 8.14536E-7
Slope	-3.15136E-6 ± 4.30295E-8
Residual Sum of Squares	2.57437E-12
Pearson's r	-0.99963
R-Square (COD)	0.99925
Adj. R-Square	0.99907

Equation	y = a + b*x
Plot	-1.14
Weight	No Weighting
Intercept	3.12745E-6 ± 7.75159E-7
Slope	-3.46049E-6 ± 4.09494E-8
Residual Sum of Squares	2.33148E-12
Pearson's r	-0.99972
R-Square (COD)	0.99944
Adj. R-Square	0.9993

Figure S27. CV's from 0→-1.9→0 V, at varying scan rates, for 1 mM MeCN solution of $[\mathrm{Co^{II}}\mathbf{L}^{\mathrm{i}}]^{2+}$, and and plots of cathodic peak current versus the square root of the scan rate ($\boldsymbol{\upsilon}^{1/2}$) for the 3 redox events at E_{pc} = -1.18 V (Diffusion coefficient, (*D*) = 3.23 × 10^{-8} cm^2 s^{-1}), E_{pc} = -1.63 V (*D* = 2.68 × 10^{-8} cm^2 s^{-1}), and E_{pc} = -1.78 V (*D* = 3.10 × 10^{-8} cm^2 s^{-1}).

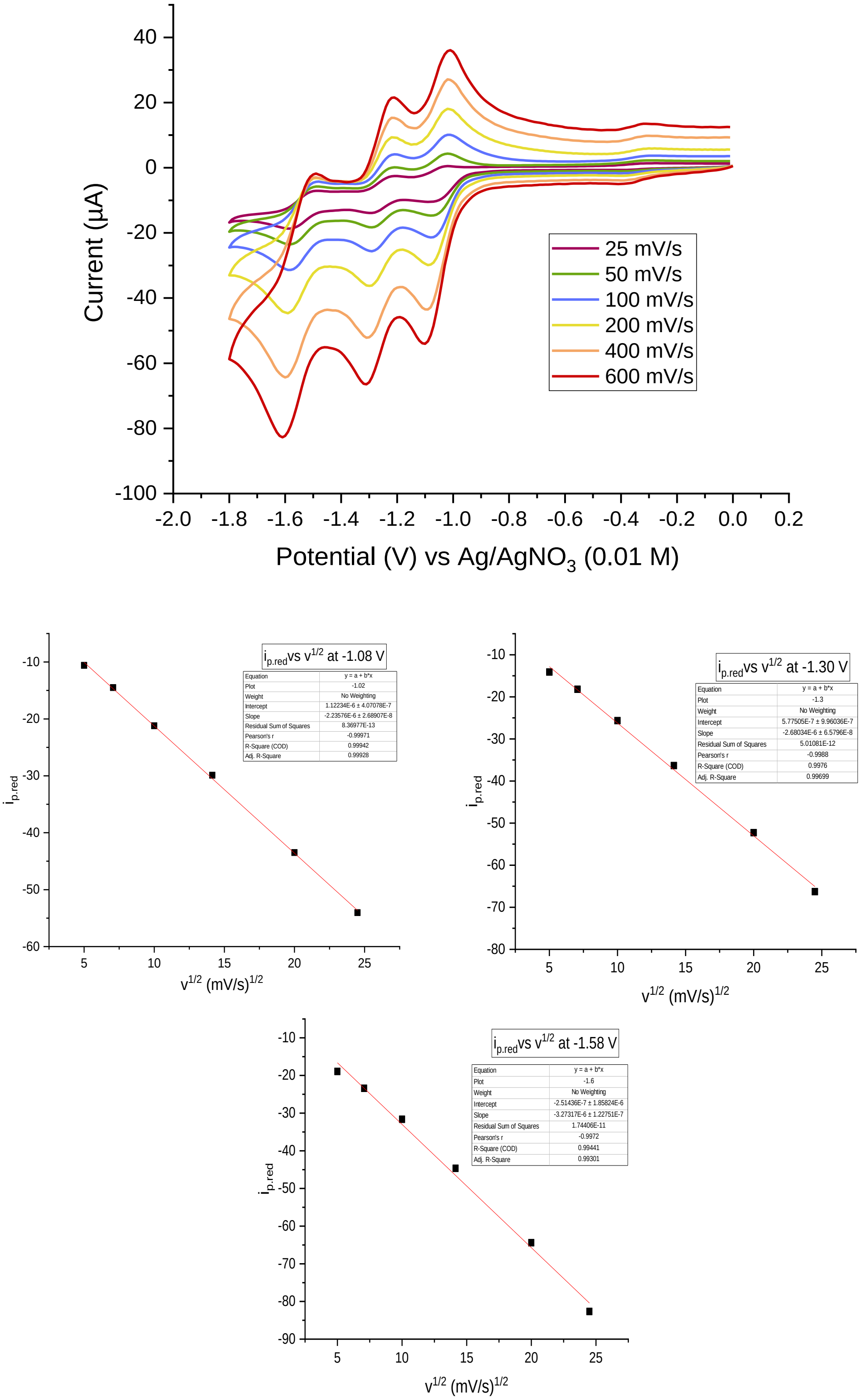

Equation	y = a + b*x
Plot	-1.02
Weight	No Weighting
Intercept	1.12234E-6 ± 4.07078E-7
Slope	-2.23576E-6 ± 2.68907E-8
Residual Sum of Squares	8.36977E-13
Pearson's r	-0.99971
R-Square (COD)	0.99942
Adj. R-Square	0.99928

Equation	y = a + b*x
Plot	-1.3
Weight	No Weighting
Intercept	5.77505E-7 ± 9.96036E-7
Slope	-2.68034E-6 ± 6.5796E-8
Residual Sum of Squares	5.01081E-12
Pearson's r	-0.9988
R-Square (COD)	0.9976
Adj. R-Square	0.99699

Equation	y = a + b*x
Plot	-1.6
Weight	No Weighting
Intercept	-2.51436E-7 ± 1.85824E-6
Slope	-3.27317E-6 ± 1.22751E-7
Residual Sum of Squares	1.74406E-11
Pearson's r	-0.9972
R-Square (COD)	0.99441
Adj. R-Square	0.99301

Figure S28. CV's from 0→-1.9→0 V, at varying scan rates, for 1 mM MeCN solution of $[\mathrm{Fe^{II}Cu^{I}}\mathbf{L}^{\mathrm{i}}]^{3+}$, and and plots of cathodic peak current versus the square root of the scan rate ($\boldsymbol{v}^{1/2}$) for the 3 redox events at E_{pc} = -1.08 V (Diffusion coefficient, (*D*) = 1.34 ×10^{-8} cm^2 s^{-1}), E_{pc} = -1.28 V (*D* = 1.94 × 10^{-8} cm^2 s^{-1}), and E_{pc} = -1.56 V (*D* = 2.89 × 10^{-8} cm^2 s^{-1}).

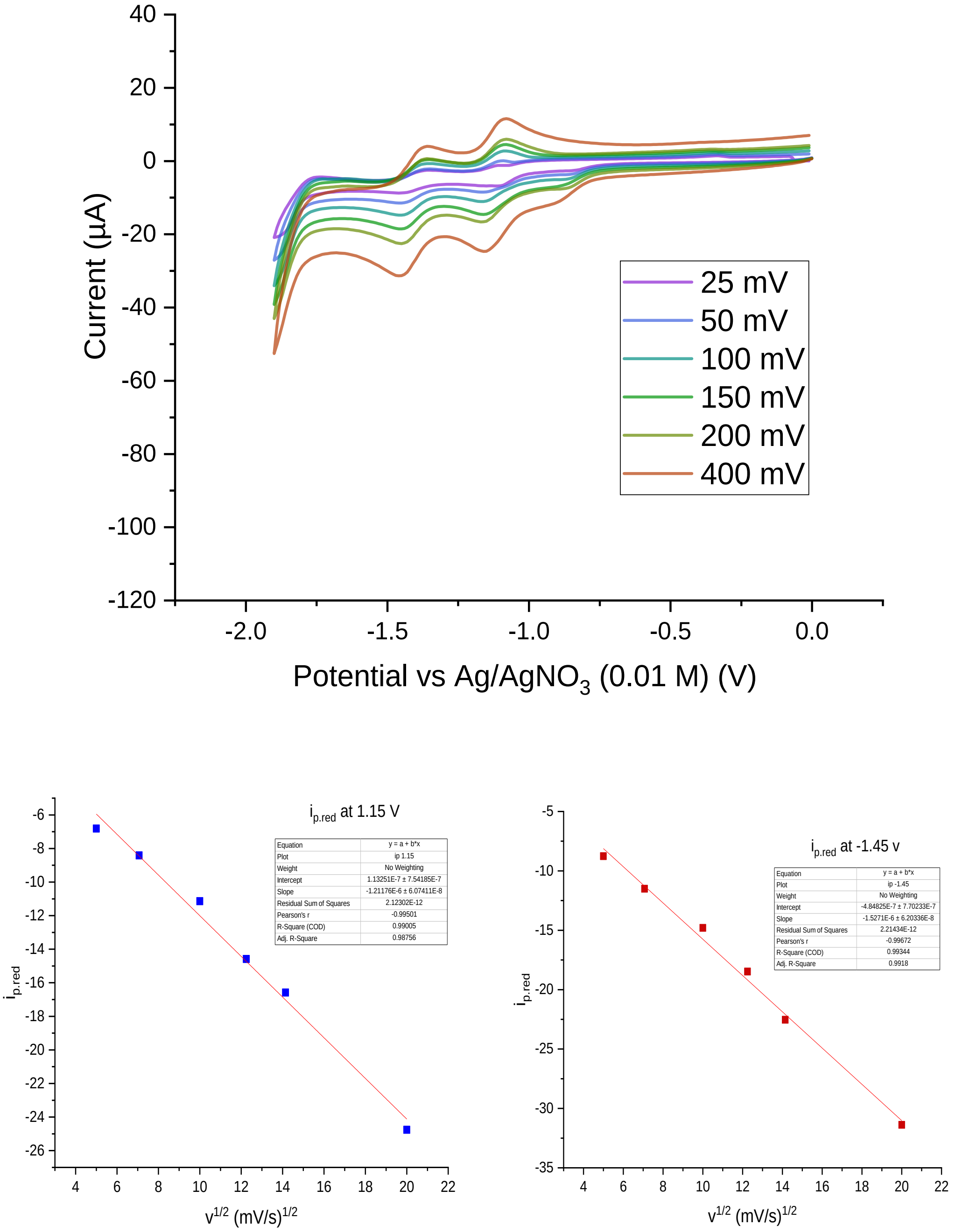

Equation	y = a + b*x
Plot	ip 1.15
Weight	No Weighting
Intercept	1.13251E-7 ± 7.54185E-7
Slope	-1.21176E-6 ± 6.07411E-8
Residual Sum of Squares	2.12302E-12
Pearson's r	-0.99501
R-Square (COD)	0.99005
Adj. R-Square	0.98756

Equation	y = a + b*x
Plot	ip -1.45
Weight	No Weighting
Intercept	-4.84825E-7 ± 7.70233E-7
Slope	-1.5271E-6 ± 6.20336E-8
Residual Sum of Squares	2.21434E-12
Pearson's r	-0.99672
R-Square (COD)	0.99344
Adj. R-Square	0.9918

Figure S29. CV's from 0→-1.9→0 V, at varying scan rates, for 1 mM MeCN solution of [Fe^{II}**L**^{i}]$^{3+}$, and and plots of cathodic peak current versus the square root of the scan rate ($\boldsymbol{v^{1/2}}$) for the 2 redox events at E_{pc} = -1.15 V (Diffusion coefficient, (*D*) = 3.95 × 10^{-9} cm^2 s^{-1}), E_{pc} = -1.45 V (Diffusion coefficient, (*D*) = 6.24 × 10^{-9} cm^2 s^{-1}).

4.2.1 Table comparing the $E_{1/2}$ values obtained herein for the 6 literature cryptates with those previously reported in the literature.

Table S7 Summary of electrochemical processes at negative potentials (at 100 mVs^{-1} vs 0.01 M $AgNO_3$/Ag) for the cryptates, comparing the data obtained herein (bold black; obtained from analysis of scans from 0 V to the negative limit and back to 0 V) with those reported previously (black; obtained from analysis of scans from 0 V to negative limit then to positive limit and back to 0 V) for the 6 literature cryptates (only $[Zn^{II}Cu^{I}\mathbf{L}^{i}]^{3+}$ and $[Zn^{II}\mathbf{L}^{i}]^{2+}$ are new).[6-8] Note: $E_{1/2}(Fc/Fc^+)$ = 0.09 ± 0.01 V with ΔE = 0.09 V in the H-cell used herein.

Cryptates		**$E_{1/2}$ (ΔE)[a] (V)**
$[Zn^{II}\mathbf{L}^{i}]^{2+}$	**This work**	**-1.18**^{IR} **1.25 (0.07)**^{QR} **-1.41 (0.07)**^{QR} **-1.50 (0.07)**^{QR} **-1.75 (0.09)** ^{QR}
	Literature	N/A (new cryptate)
$[Cu^{II}\mathbf{L}^{i}]^{2+}$	**This work**	**-0.34 (0.09)**^{R} **-1.39 (0.11)**
	Literature	-0.38 (0.08) -1.37^{QR}
$[Co^{II}\mathbf{L}^{i}]^{2+}$	**This work**	**-1.14 (0.08)**^{QR} **-1.58 (0.10)**^{R} **-1.72 (0.11)**^{R}
	Literature	-1.14 (0.07) -1.56 (0.08) -1.71^{QR}
$[Fe^{II}\mathbf{L}^{i}]^{2+}$	**This work**	**-1.11 (0.08)**^{R} **-1.40 (0.09)**^{R} **-1.84 (0.13)**^{QR}
	Literature	-1.13 (0.07) -1.42 (0.07) -1.87 (0.11)^{QR}
$[Zn^{II}Cu^{I}\mathbf{L}^{i}]^{3+}$	**This work**	**-1.05**^{IR} **-1.24 (0.10)**^{R} **-1.49 (0.09)**^{R} **-1.79 (0.10)**^{R}
	Literature	N/A (new cryptate)
$[Cu^{II}Cu^{I}\mathbf{L}^{i}]^{3+}$	**This work**	**-0.32 (0.10)**^{R} **-1.08 (0.05)** **-1.24 (0.10)**^{R} **-1.43 (0.17)**^{QR} **-1.92 (0.12)**^{QR}
	Literature	-0.34 (0.08) [b] -1.27^{QR} -1.44^{QR} -1.98^{QR}
$[Co^{II}Cu^{I}\mathbf{L}^{i}]^{3+re}$	**This work**	**-0.95 (0.17)** **-1.14 (0.08)**^{QR} **-1.42 (0.08)**^{OR} **-1.56 (0.08)**^{OR} **-1.71 (0.10)**
	Literature	-0.88 (0.06)^{QR} -1.15 (0.07)^{QR} -1.41 (0.10)^{QR} -1.55 (0.08)^{QR} [b]
$[Fe^{II}Cu^{I}\mathbf{L}^{i}]^{3+}$	**This work**	**-1.04 (0.08)**^{R} **-1.25(0.09)**^{R} **-1.54 (0.10)**^{R} **-1.84**^{QR}
	Literature	-1.07 (0.09) -1.27 (0.07) -1.55 (0.07) -1.89^{QR}

[a] IR = irreversible so the value provided is E_{pc}; R = reversible; QR = quasi-reversible based using $\Delta E(Fc^+/Fc)$ = 0.09 V as the standard for a reversible process in the cell used herein. [b] not reported in literature CV, but was scanned over a different range.

4.2.2 Diffusion coefficient calculations

To calculate the diffusion coefficient, *D*, the Randles–Sevcik equation[9] is:

$$i_p \quad = 0.4463nFAC^0 \left(\frac{nF\upsilon D}{RT}\right)^{\frac{1}{2}} \qquad (1)$$

<u>Where</u>

i_p is the peak current (A),

n is number of electrons transferred,

A is electrode surface area (cm^2),

C^0 is analyte concentration (mol cm^{-3}),

υ is scan rate (V/s),

D is diffusion coefficient (cm^2 s^{-1}),

F is Faraday's constant (C mol^{-1}),

R is gas constant (J K^{-1} mol^{-1}) and

T is temperature (K).

Rearranging eqn 1 slightly gives:

$$i_p \quad = \left[0.4463nFAC^0 \left(\frac{nFD}{RT}\right)^{1/2}\right] \upsilon^{\frac{1}{2}}$$

So the slope of a plot of $i_p$versus $\upsilon^{\frac{1}{2}}$ is given by:

$$slope \quad = 0.4463nFAC^0 \left(\frac{nFD}{RT}\right)^{\frac{1}{2}} \qquad (2)$$

Enabling easy calculation of *D* the diffusion coefficient from the slope by rearranging eqn 2:

$$D \ = \left(\frac{slope}{0.4463nFAC^0}\right)^2 \frac{RT}{nF}$$

Then substituting n = 1, A = 0.071 cm^2, C^0 = 1x10^{-6} (mol cm^{-3}), F = 96,485 (C mol^{-1}), R = 8.314(J K^{-1} mol^{-1} and T = 293 K:

$$\underline{D \ = 2700(slope)^2 \ \text{cm}^2\text{s}^{-1}}$$

Table S8 Diffusion coefficients (D, cm^{2}s^{-1}) calculated using Randles–Sevcik equation[9, 10] (previous section), from the slopes in the plots of square root of scan rate vs peak cathodic current (Figure S23-S29) at each E_{pc} noted for each of the cryptates.

	Heterobinuclear cryptates				**Mononuclear cryptates**			
	$[Zn^{II}Cu^{I}L^{i}]^{3+}$				**$[Zn^{II}L^{i}]^{2+}$**			
E_{pc}(V)	-1.29	-1.54	-1.84		-1.28	-1.45	-1.54	-1.82
D, cm^{2}s^{-1}	1.52×10^{-8}	1.94×10^{-8}	3.64×10^{-8}		9.04×10^{-9}	1.08×10^{-8}	1.69×10^{-8}	2.76×10^{-8}
	$[Fe^{II}Cu^{I}L^{i}]^{3+}$				**$[Fe^{II}L^{i}]^{2+}$**			
E_{pc} (V)	-1.08	-1.28	-1.56		-1.15	-1.45		
D, cm^{2}s^{-1}	1.34×10^{-8}	1.94×10^{-8}	2.89×10^{-8}		3.95×10^{-9}	6.24×10^{-9}		
	$[Co^{II}Cu^{I}L^{i}]^{3+}$				**$[Co^{II}L^{i}]^{2+}$**			
E_{pc} (V)	-1.11	-1.46	-1.59	-1.76	-1.18	-1.63	-1.78	
D, cm^{2}s^{-1}	1.67×10^{-8}	1.25×10^{-8}	2.37×10^{-8}	3.03×10^{-8}	3.23×10^{-8}	2.68×10^{-8}	3.10×10^{-8}	
	$[Cu^{II}Cu^{I}L^{i}]^{3+}$				**$[Cu^{II}L^{i}]^{2+}$**			
E_{pc} (V)	-0.34	-1.29	-1.52	-1.77	-0.40			
D, cm^{2}s^{-1}	9.75×10^{-9}	1.07×10^{-8}	1.94×10^{-8}	1.67×10^{-8}	1.92×10^{-8}			

4.3 CVs with successive additions of acetic acid

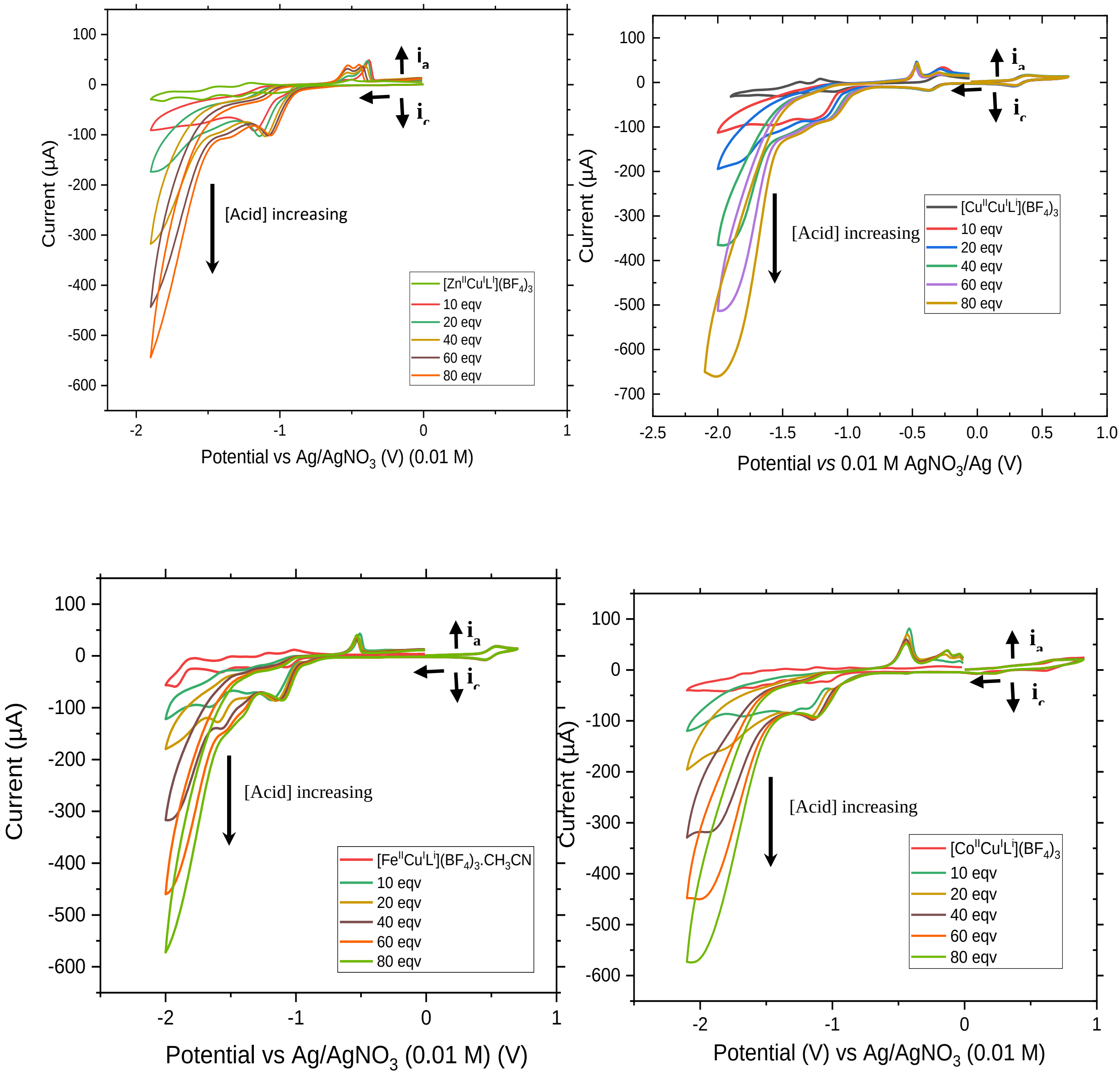

Figure S30. CVs, 0 → −2.0 ± 0.2 → 0 V *vs*. 0.01 M $AgNO_3$/Ag, for a 1 mM MeCN solution of $[Zn^{II}Cu^{I}\mathbf{L}^{i}]^{3+}$ (top left), $[Cu^{II}Cu^{I}\mathbf{L}^{i}]^{3+}$ (top right), $[Fe^{II}Cu^{I}\mathbf{L}^{i}]^{3+}$ (bottom left), and $[Co^{II}Cu^{I}\mathbf{L}^{i}]^{3+}$ (bottom right) all with successive additions of 10 or 20 equivalents of acetic acid, up to a total of 80 equivalents = 80 mM, with increasing [acid] leading to increasing catalytic wave currents. Conditions: 0.1 M $(NBu_4)PF_6$, glassy carbon working electrode (d = 3 mm, A = 0.071 cm^2), scan rate 100 mVs^{-1}.

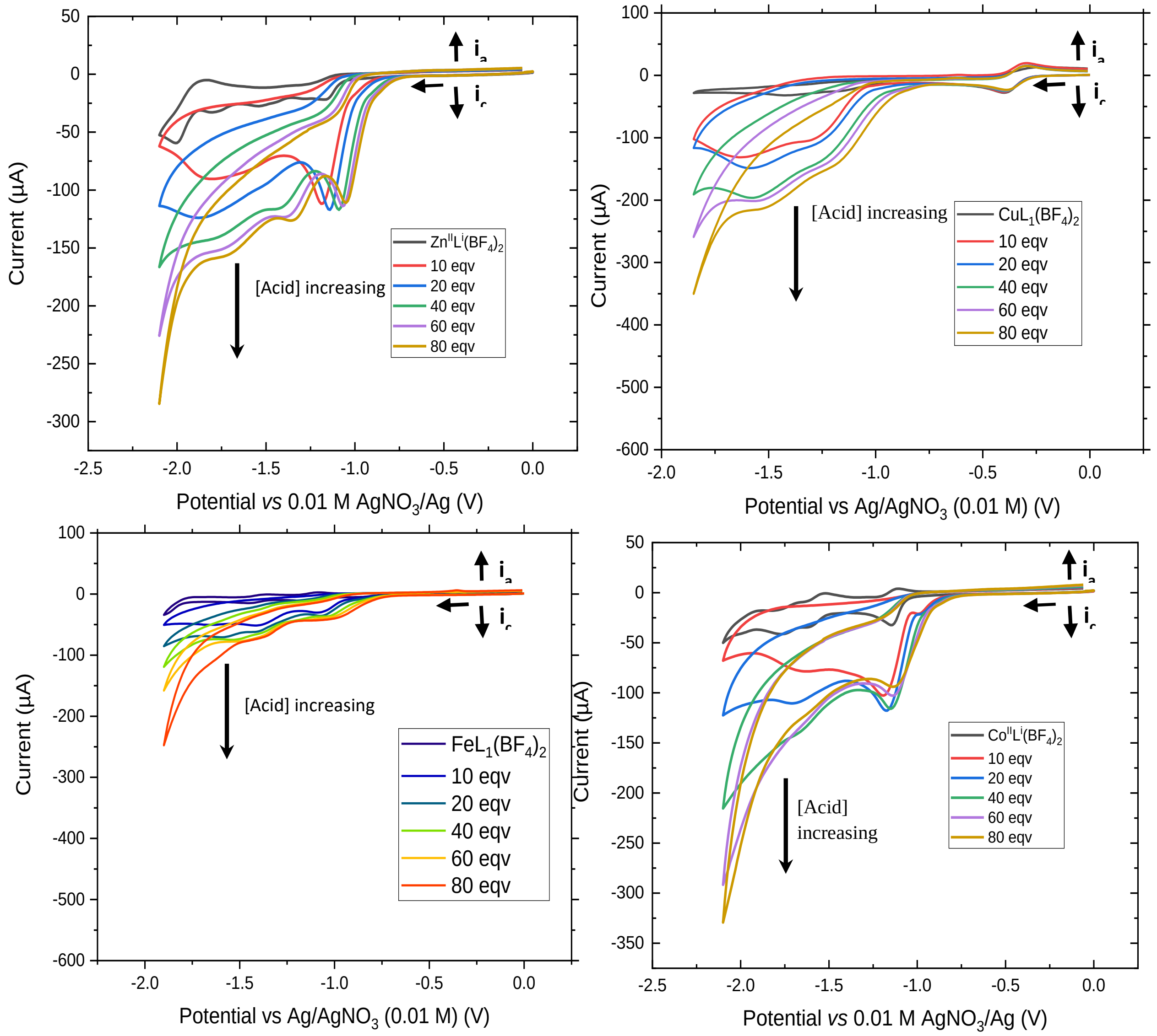

Figure S31. CVs, 0 → −2.0 ± 0.2 → 0 V *vs*. 0.01 M AgNO$_3$/Ag, for a 1 mM MeCN solution of [Zn^{II}**L**^{i}]$^{2+}$ (top left), [Cu^{II}**L**^{i}]$^{2+}$(top right), [Fe^{II}**L**^{i}]$^{2+}$ (bottom left), and [Co^{II}**L**^{i}]$^{2+}$ (bottom right) all with successive additions of 10 or 20 equivalents of acetic acid, up to a total of 80 equivalents = 80 mM, with increasing [acid] leading to increasing catalytic wave currents. Conditions: 0.1 M (NBu$_4$)PF$_6$, glassy carbon working electrode (*d* = 3 mm, *A* = 0.071 cm^2), scan rate 100 mVs^{-1}.

4.4 Controlled potential electrolysis of cryptates and controls, at -1.6 V, and rinse tests

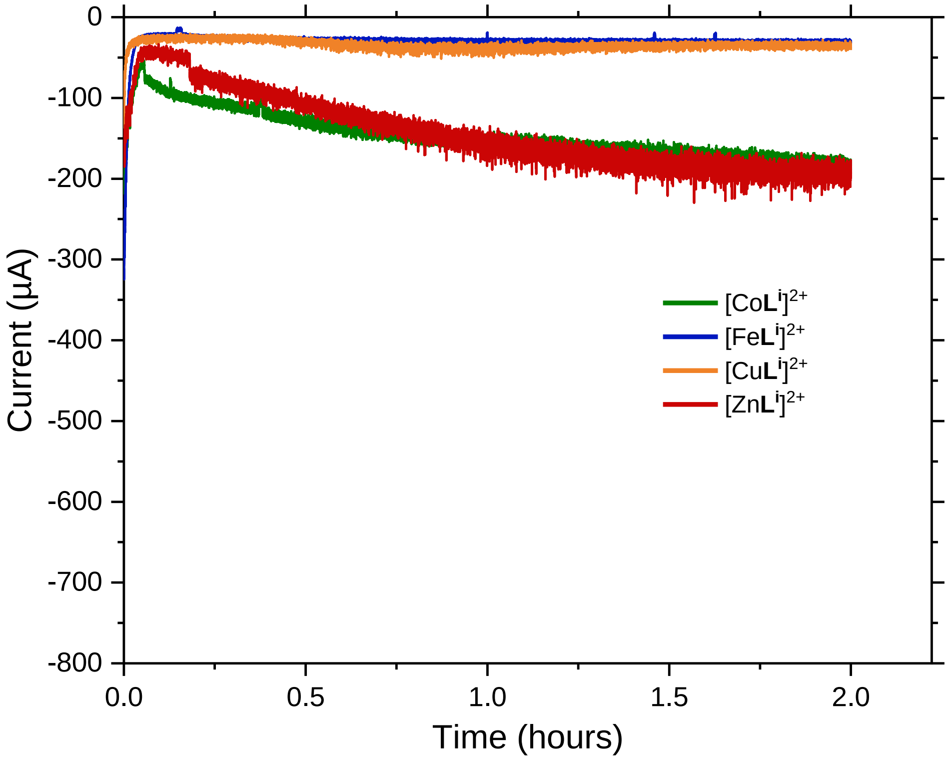

Figure S32. Controlled potential electrolysis (CPE) at −1.60 V of an 8 mL solution of 80 mM acetic acid in the presence of 1 mM of [Zn^{II}**L**^{i}]$^{2+}$ (green), [Cu^{II}**L**^{i}]$^{2+}$ (navy blue), [Fe^{II}**L**^{i}]$^{2+}$ (orange), and [Co^{II}**L**^{i}]$^{2+}$ (red).

$[Fe^{II}Cu^{I}\mathbf{L^{i}}]^{3+}$ **CPE** at -1.6 V

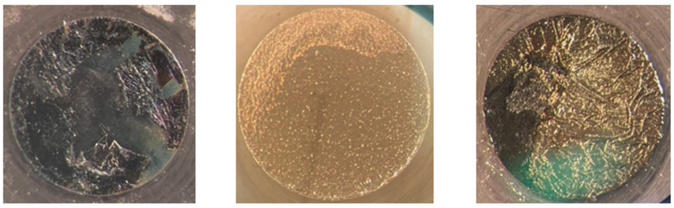

$[Fe^{II}Cu^{I}\mathbf{L^{i}}]^{3+}$ run 2 $[Fe^{II}Cu^{I}\mathbf{L^{i}}]^{3+}$ run 3 $[Fe^{II}Cu^{I}\mathbf{L^{i}}]^{3+}$ run 4

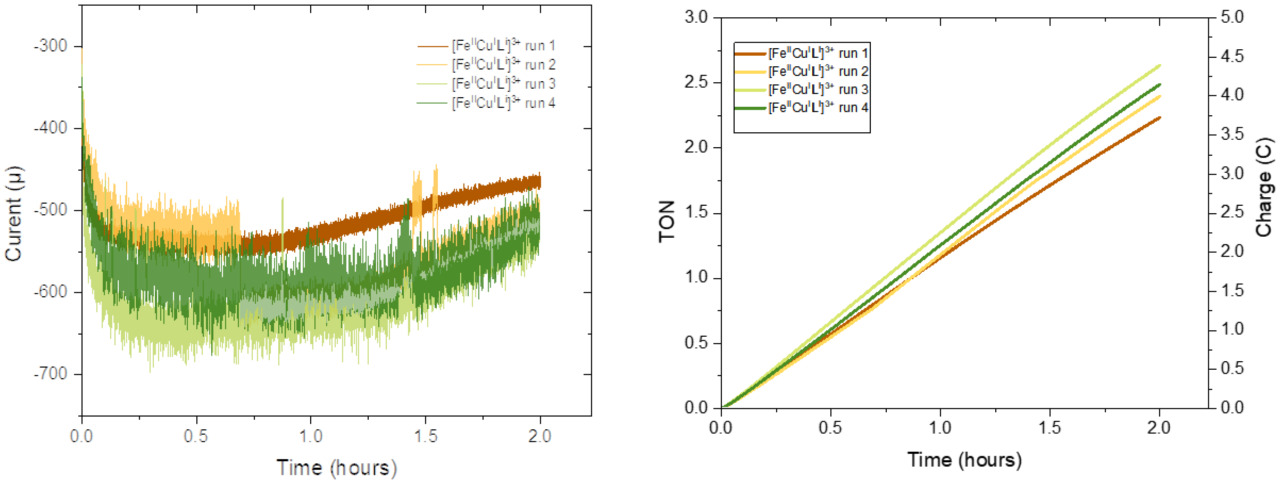

Figure S33. Multiple CPE experiments at −1.60 V on an 8 mL solution of 80 mM acetic acid in the presence of 1 mM of $[Fe^{II}Cu^{I}\mathbf{L^{i}}]^{3+}$ showing similar activity (left), with pictures on top showing the deposits on the working electrode after 2 hours of CPE. (Right) The plot providing total charge transferred and TON for each CPE experiment. Conditions: 0.1 M $(NBu_4)PF_6$, glassy carbon working electrode (*d* = 3 mm, *A* = 0.071 cm^2), scan rate 100 mVs^{-1}.

$[Fe^{II}Cu^{I}\mathbf{L}^{i}]^{3+}$ **rinse test CPE** at -1.6 V

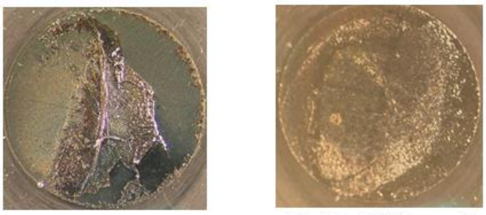

$[Fe^{II}Cu^{I}\mathbf{L}^{i}]^{3+}$ run 3 $[Fe^{II}Cu^{I}\mathbf{L}^{i}]^{3+}$ run 4

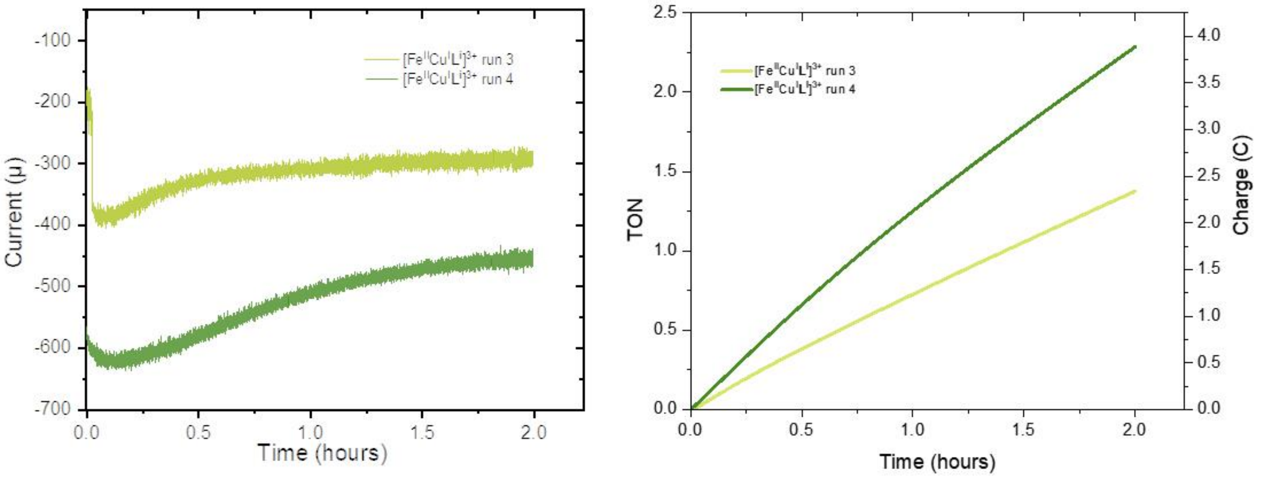

Figure S34. Two rinse test CPE experiments for $[Fe^{II}Cu^{I}\mathbf{L}^{i}]^{3+}$ at −1.60 V in presence of 80 mM acetic acid in 0.1 M $(NBu_4)PF_6$ solution (left), with pictures on top showing the deposits on the working electrode after 2 hours of the rinse test. (Right) The plot providing total charge transferred and TON for each rinse test. Conditions: glassy carbon working electrode (*d* = 3 mm, *A* = 0.071 cm^2), scan rate 100 mVs^{-1}.

$[Co^{II}Cu^{I}\mathbf{L}^{i}]^{3+}$ **CPE** at -1.6 V

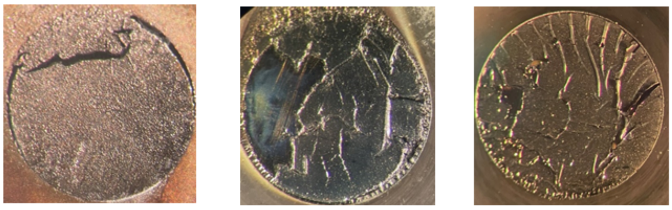

$[Co^{II}Cu^{I}\mathbf{L}^{i}]^{3+}$ run 1 $[Co^{II}Cu^{I}\mathbf{L}^{i}]^{3+}$ run 2 $[Co^{II}Cu^{I}\mathbf{L}^{i}]^{3+}$ run 3

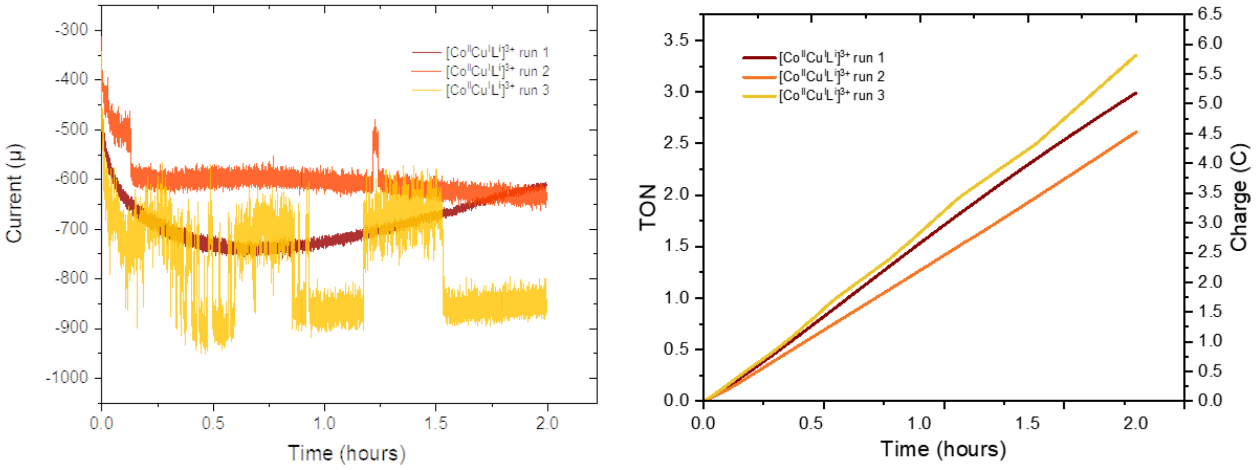

Figure S35. Multiple CPE experiments at −1.60 V on an 8 mL solution of 80 mM acetic acid in the presence of 1 mM of $[Co^{II}Cu^{I}\mathbf{L}^{i}]^{3+}$ with two runs (run 1 and run 2) showing similar activity and run 3 showing slightly higher activity but within the experimental errors (left), with pictures on top showing the deposits on the working electrode after 2 hours of CPE. (Right) The plot providing total charge transferred and TON for each CPE experiment. Conditions: 0.1 M $(NBu_4)PF_6$, glassy carbon working electrode (*d* = 3 mm, *A* = 0.071 cm^2), scan rate 100 mVs^{-1}.

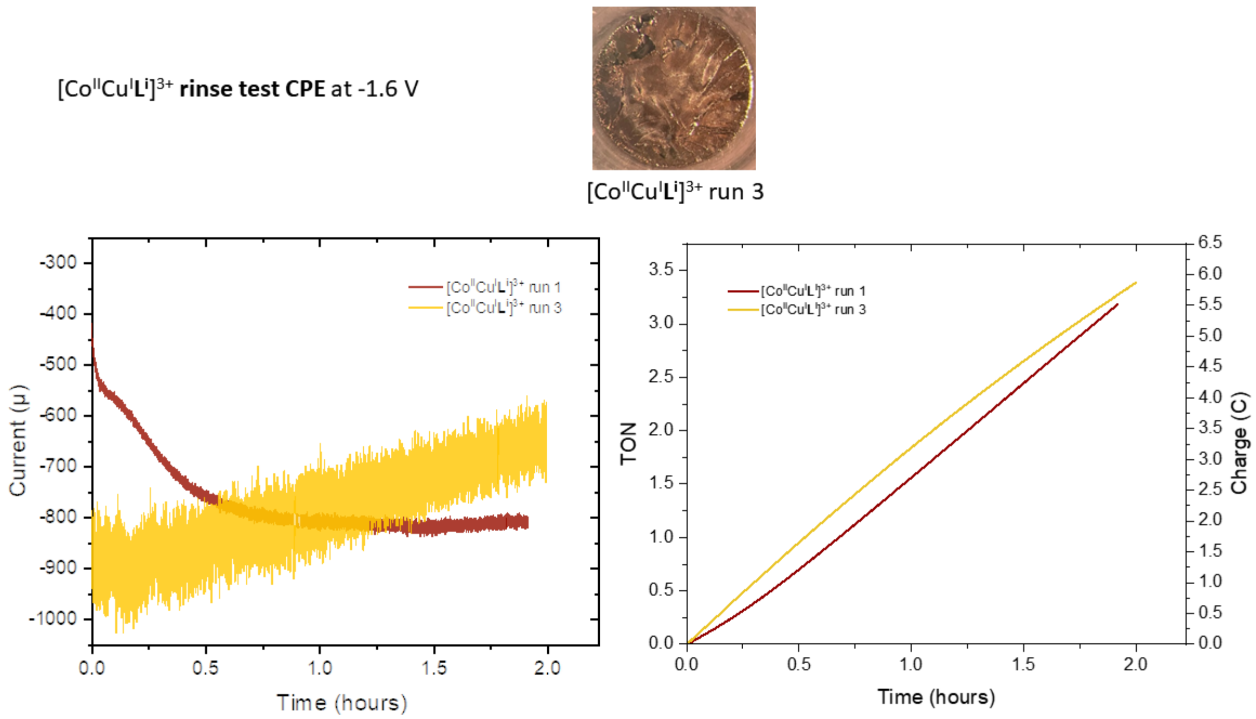

Figure S36. Two rinse test CPE experiments for $[\mathrm{Co^{II}Cu^{I}}\mathbf{L^{i}}]^{3+}$ at −1.60 V in presence of 80 mM acetic acid in 0.1 M $(\mathrm{NBu_4})\mathrm{PF_6}$ solution (left), with pictures on top showing the deposits on the working electrode after 2 hours of the rinse test. (Right) The plot providing total charge transferred and TON for each rinse test. Conditions: glassy carbon working electrode (*d* = 3 mm, *A* = 0.071 cm^2), scan rate 100 mVs^{-1}.

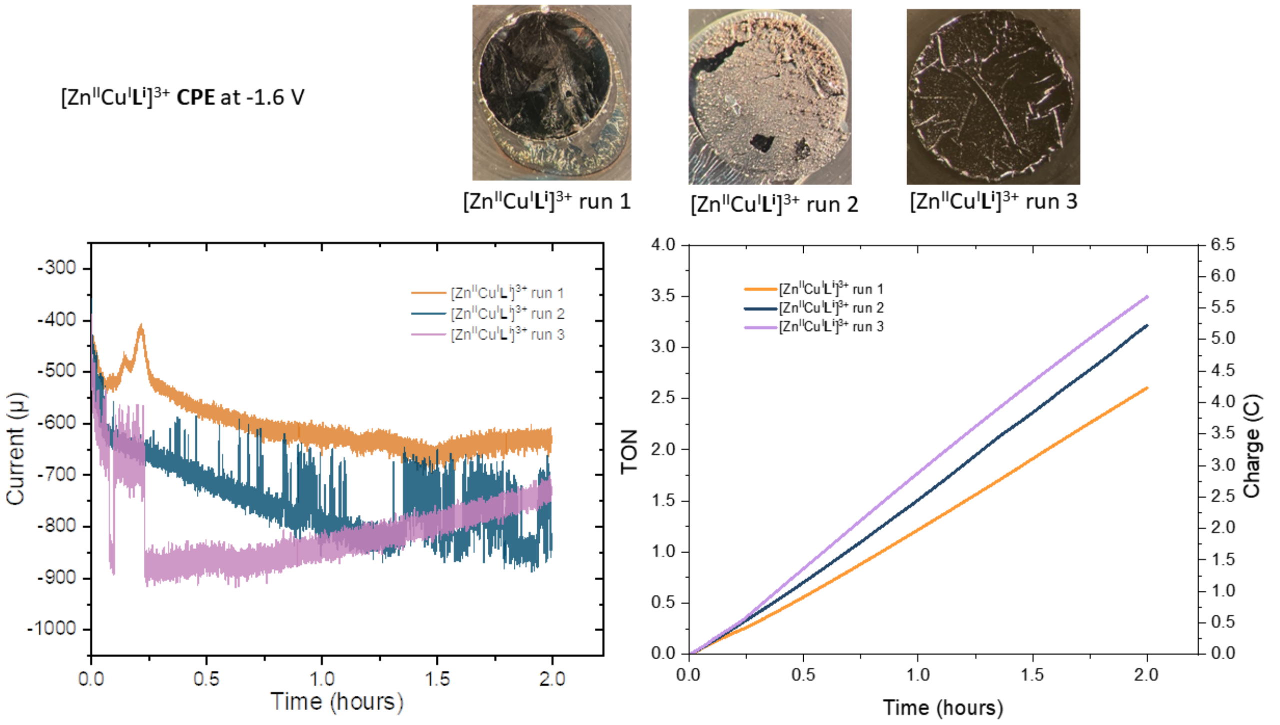

Figure S37. Multiple CPE experiments at −1.60 V on an 8 mL solution of 80 mM acetic acid in the presence of 1 mM of [Zn^{II}Cu^{I}**L^{i}**]$^{3+}$ showing similar activity within experimental errors (left), with pictures on top showing the deposits on the working electrode after 2 hours of CPE. (Right) The plot providing total charge transferred and TON for each CPE experiment. Conditions: 0.1 M $(NBu_4)PF_6$, glassy carbon working electrode (*d* = 3 mm, *A* = 0.071 cm^2), scan rate 100 mVs^{-1}.

$[Zn^{II}Cu^{I}\mathbf{L}^{i}]^{3+}$ **rinse test CPE** at -1.6 V

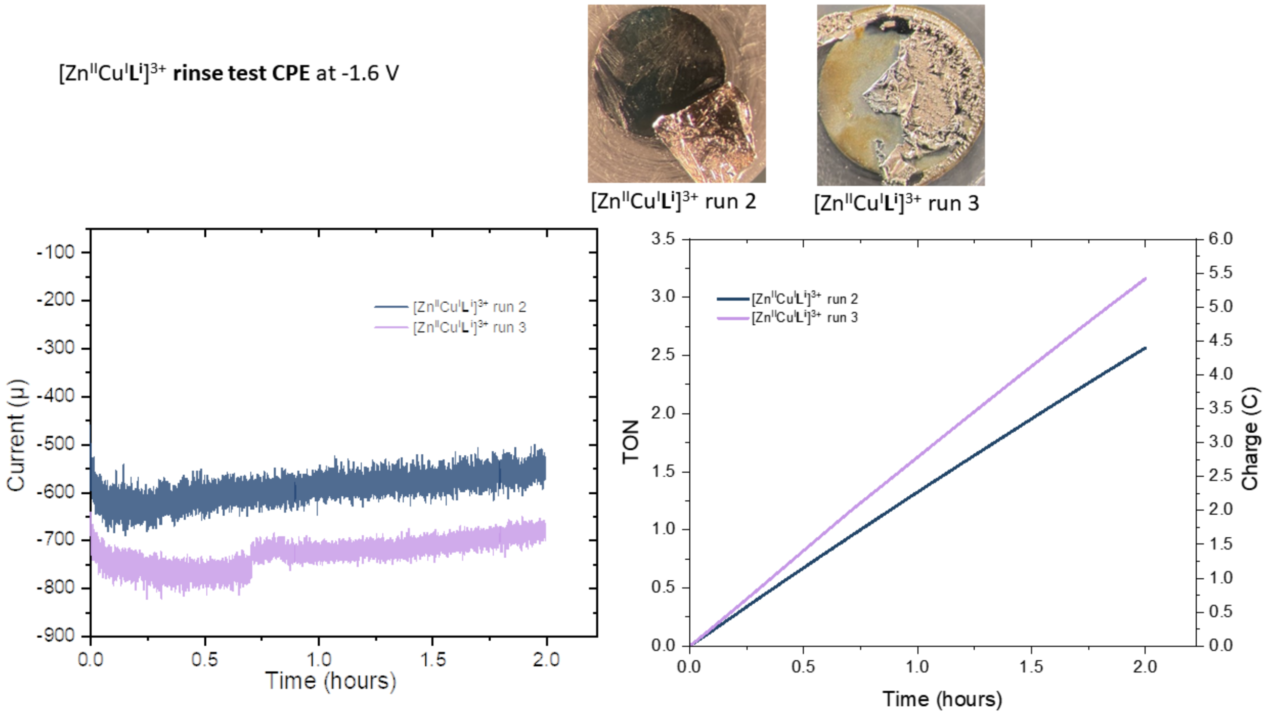

Figure S38. Two rinse test CPE experiments for $[Zn^{II}Cu^{I}\mathbf{L}^{i}]^{3+}$ at −1.60 V in presence of 80 mM acetic acid in 0.1 M $(NBu_4)PF_6$ solution (left), with pictures on top showing the deposits on the working electrode after 2 hours of the rinse test. (Right) The plot providing total charge transferred and TON for each rinse test. Conditions: glassy carbon working electrode (*d* = 3 mm, *A* = 0.071 cm^2), scan rate 100 mVs^{-1}.

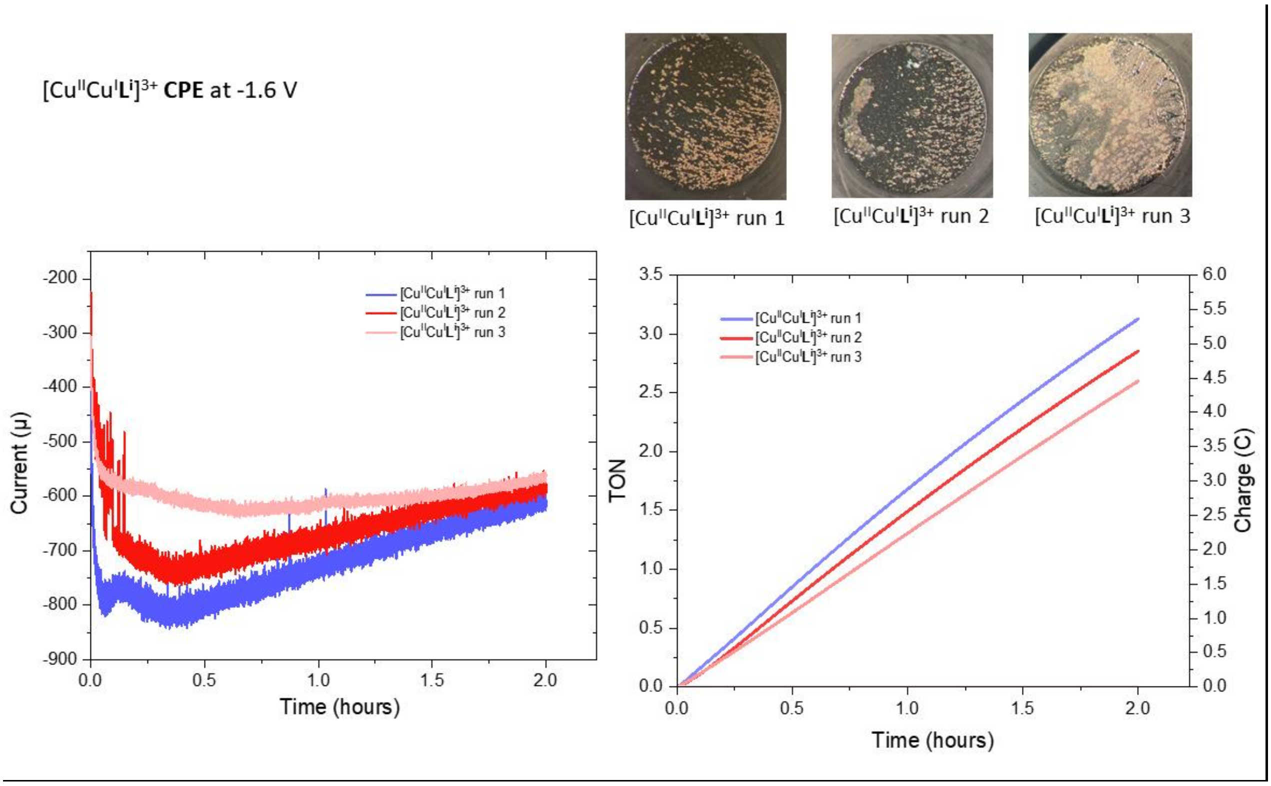

[Cu^{II}Cu^{I}**L^{i}**]$^{3+}$ **CPE** at -1.6 V

[Cu^{II}Cu^{I}**L^{i}**]$^{3+}$ run 1 [Cu^{II}Cu^{I}**L^{i}**]$^{3+}$ run 2 [Cu^{II}Cu^{I}**L^{i}**]$^{3+}$ run 3

Figure S39. Multiple CPE experiments at −1.60 V on an 8 mL solution of 80 mM acetic acid in the presence of 1 mM of [Cu^{II}Cu^{I}**L^{i}**]$^{3+}$ showing similar activity within experimental errors (left), with pictures on top showing the deposits on the working electrode after 2 hours of CPE. (Right) The plot providing total charge transferred and TON for each CPE experiment. Conditions: 0.1 M (NBu$_4$)PF$_6$, glassy carbon working electrode (*d* = 3 mm, *A* = 0.071 cm^2), scan rate 100 mVs^{-1}.

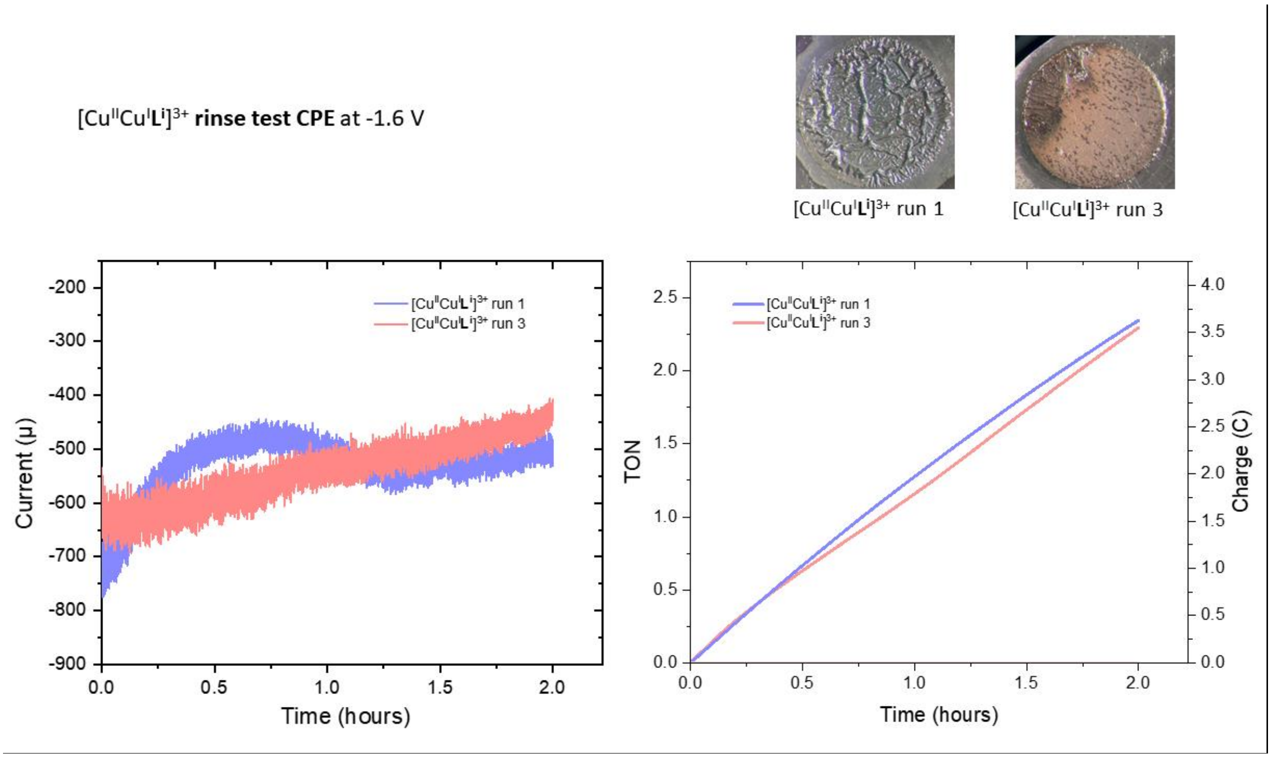

Figure S40. Two rinse test CPE experiments for $[\mathrm{Cu^{II}Cu^{I}}\mathbf{L}^{i}]^{3+}$ at −1.60 V in presence of 80 mM acetic acid in 0.1 M $(\mathrm{NBu_4})\mathrm{PF_6}$ solution (left), with pictures on top showing the deposits on the working electrode after 2 hours of the rinse test. (Right) The plot providing total charge transferred and TON for each rinse test. Conditions: glassy carbon working electrode (d = 3 mm, A = 0.071 cm^2), scan rate 100 mVs^{-1}.

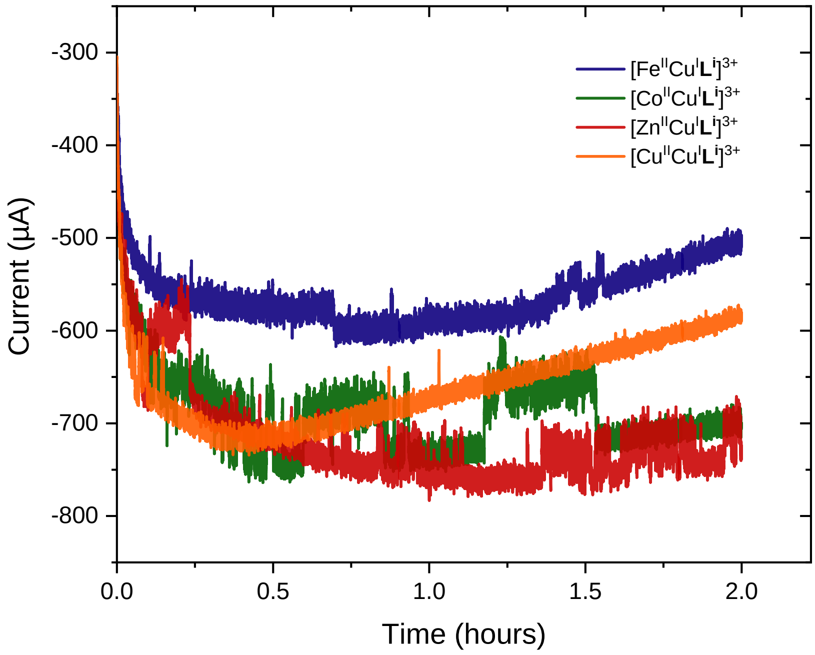

Figure S41. The averaged CPE data (see above Figures for individual runs) at -1.60 V of an 8 mL solution of 80 mM acetic acid in the presence of 1 mM of $[\mathrm{Fe^{II}Cu^{I}}\mathbf{L}^{i}]^{3+}$ (navy blue), $[\mathrm{Co^{II}Cu^{I}}\mathbf{L}^{i}]^{3+}$ (green), $[\mathrm{Zn^{II}Cu^{I}}\mathbf{L}^{i}]^{3+}$ (red), and $[\mathrm{Cu^{II}Cu^{I}}\mathbf{L}^{i}]^{3+}$ orange).

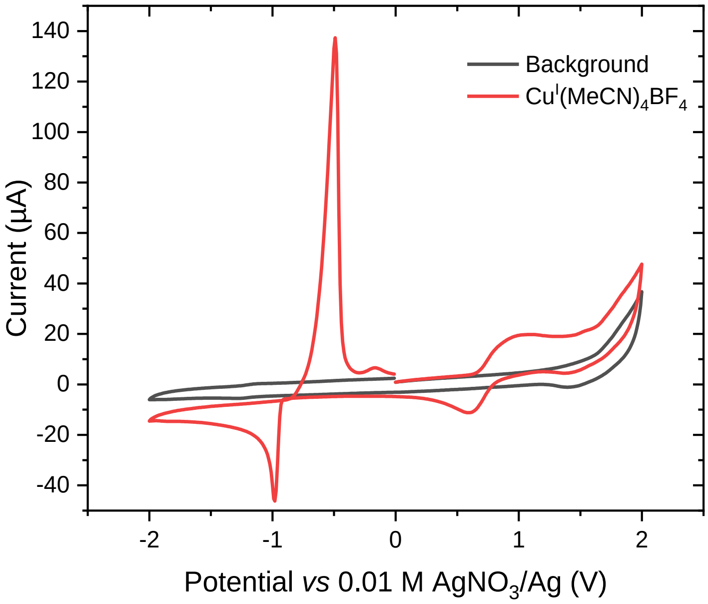

Figure S42. CV, 0→ 2.0→ -2.0→ 0 V vs 0.01 M $AgNO_3$/Ag, for a 1 mM MeCN solution of $Cu^I(MeCN)_4BF_4$ (red) and background (black). Conditions: 0.1 M $(NBu_4)PF_6$, glassy carbon working electrode (d = 3 mm, A = 0.071 cm2), scan rate 100 mVs^{-1}.

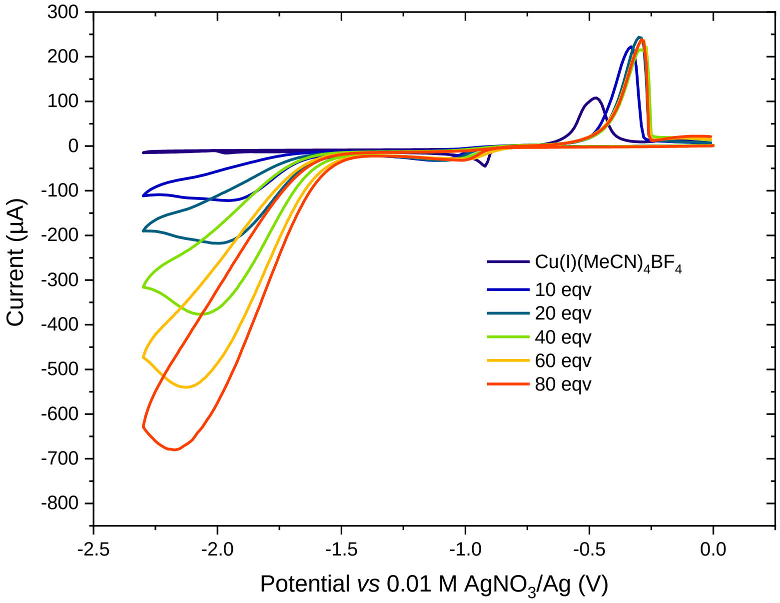

Figure S43. CVs, 0→ -2.3→ 0 V vs 0.01 M AgNO3/Ag, for a 1 mM MeCN solution of $Cu^I(MeCN)_4BF_4$, with successive additions of 10 or 20 equivalents of acetic acid (see key), up to a total of 80 equivalents = 80 mM. Conditions: 0.1 M $(NBu_4)PF_6$, glassy carbon working electrode (d = 3 mm, A = 0.071 cm^2), scan rate 100 mVs^{-1}.

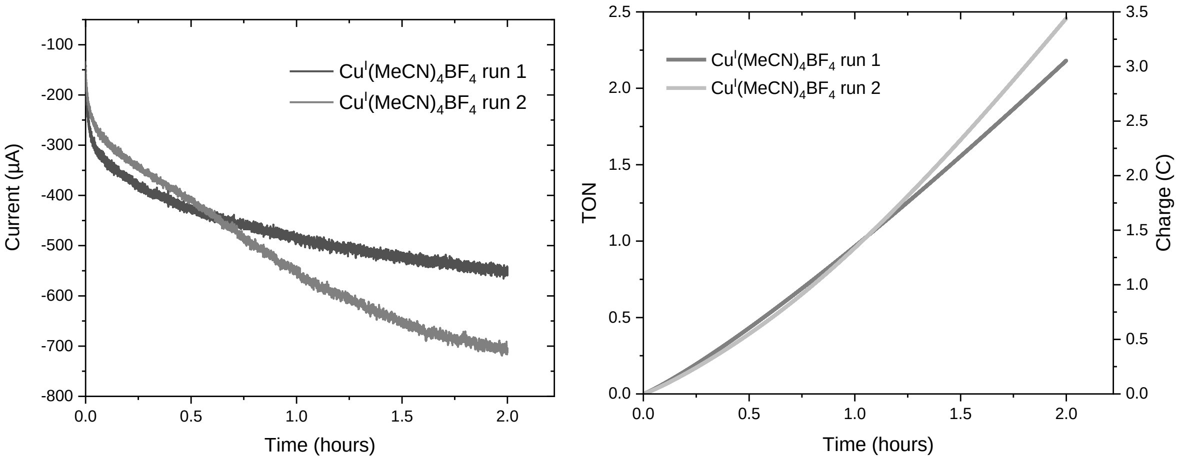

Figure S44. (Left) Multiple CPE experiments at −1.60 V on an 8 mL solution of 80 mM acetic acid in the presence of 1 mM of [$Cu^I(MeCN)_4BF_4$] over 2 hours showing similar activity within experimental errors. (Right) The plot providing total charge transferred and TON for each CPE experiment. Conditions: 0.1 M $(NBu_4)PF_6$, glassy carbon working electrode (d = 3 mm, A = 0.071 cm^2), scan rate 100 mVs^{-1}.

4.5 Repeat of CVs and CPE on literature complex [Cu^{II}**L**^{Et}](BF$_4$); pretreatment of electrode

Given [Cu^{II}**L**^{Et}](BF$_4$) has been studied in depth as an HER electrocatalyst,[11, 12] it was used as a reference compound for the present study. But when the CV of [Cu^{II}**L**^{Et}](BF$_4$) was carried out to test that the new sample of this literature complex[13] was pure, an additional bump was persistent in the CV (Figure S45, dark blue curve), regardless of our confidence in the purity of the sample. The 'bump' reduced in size on subsequent scans (Figure S45, other curves), becoming negligible by about the 5th cycle (Figure S45, red curve) but this was unsatisfactory.

Hence the working electrode was instead pre-treated, to remove any adsorbed species, as recommended by Dempsey and co-workers.[10] This involved first running five CVs with the glassy carbon electrode in a blank electrolyte solution, 0→ 2.0→ -2.0→ 0 V vs 0.01 M AgNO$_3$/Ag (Figure S46).

Only after doing that was the working electrode used to obtain CVs in the working solution of the complex of interest, in this case [Cu^{II}**L**^{Et}]BF$_4$, which resulted in the desired outcome, a CV with no 'bump' present (Figure S47, orange curve).

This study highlights the importance of pre-treating the electrode, as recommended by Dempsey and co-workers,[10] before running electrochemistry experiments.

CPE runs on this literature [Cu^{II}**L**^{Et}](BF$_4$) complex were also repeated herein, as this complex provides a useful reference system for the present studies. Lower HER activity than that reported (7.3 C, and TON$_{2h}$ = 4.7)[12] was consistently observed herein (4.2 C and TON$_{2h}$ = 2.4; Figure S48). Furthermore, visible deposits were noted during and after CPE, either on the glassy carbon working electrode or detaching from the working electrode and floating to the bottom of the cell (Figure S48). This is consistent with the results seen more recently for this complex in water,[11] providing further evidence that, like in water, the active catalyst in acetic acid/MeCN is also likely to be the heterogenous product formed from decomposition of the cryptate – not the cryptate itself.

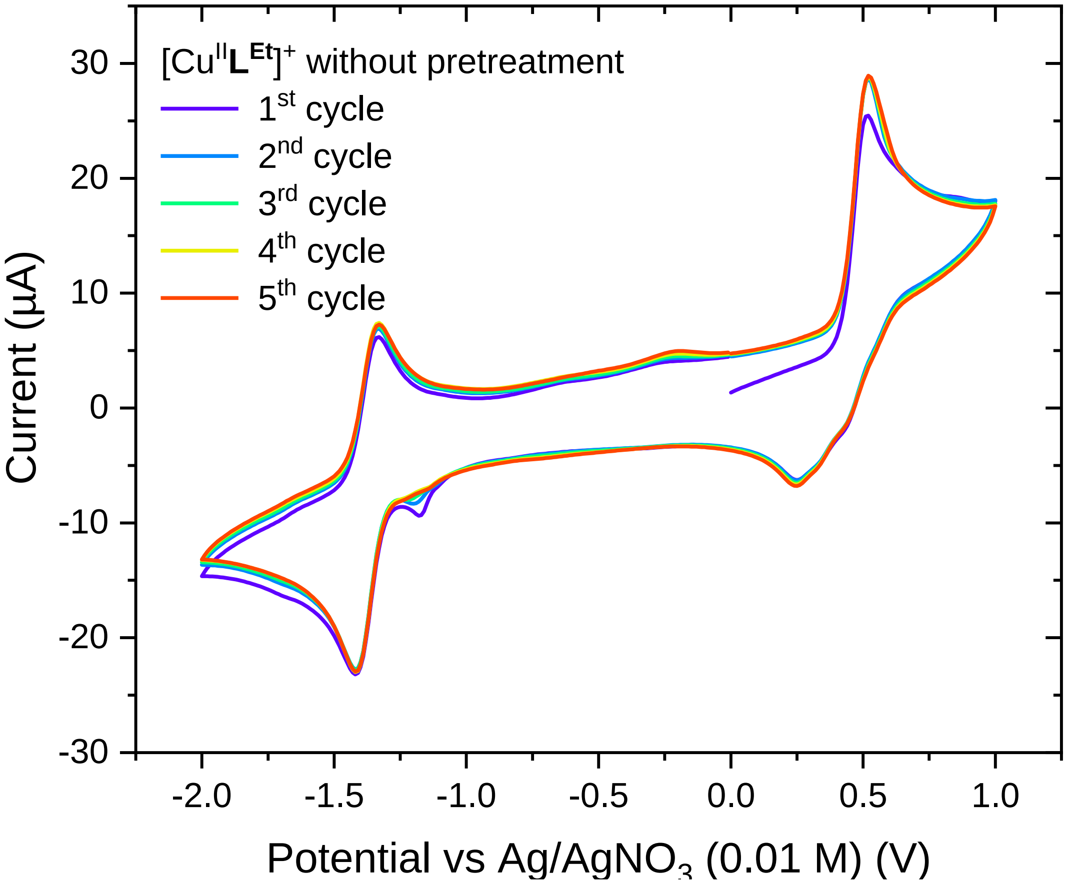

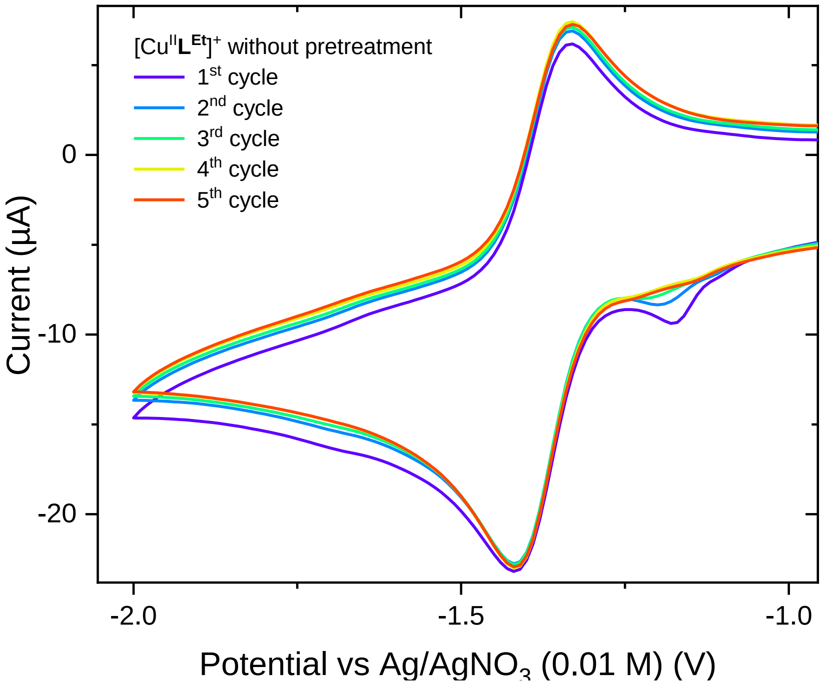

Figure S45. (Top) Five cycles of CVs without pretreatment, 0→ 1.0→ -2.0→ 0 V vs 0.01 M $AgNO_3$/Ag, for a 1 mM MeCN solution of [Cu^{II}**L**^{Et}]BF_4. Conditions: 0.1 M $(NBu_4)PF_6$, glassy carbon working electrode (d = 3 mm, A = 0.071 cm^2), scan rate 100 mVs^{-1}. (Bottom) Zoomed up CV showing the redox process with the 'bump' on it diminishing as the cycles continued.

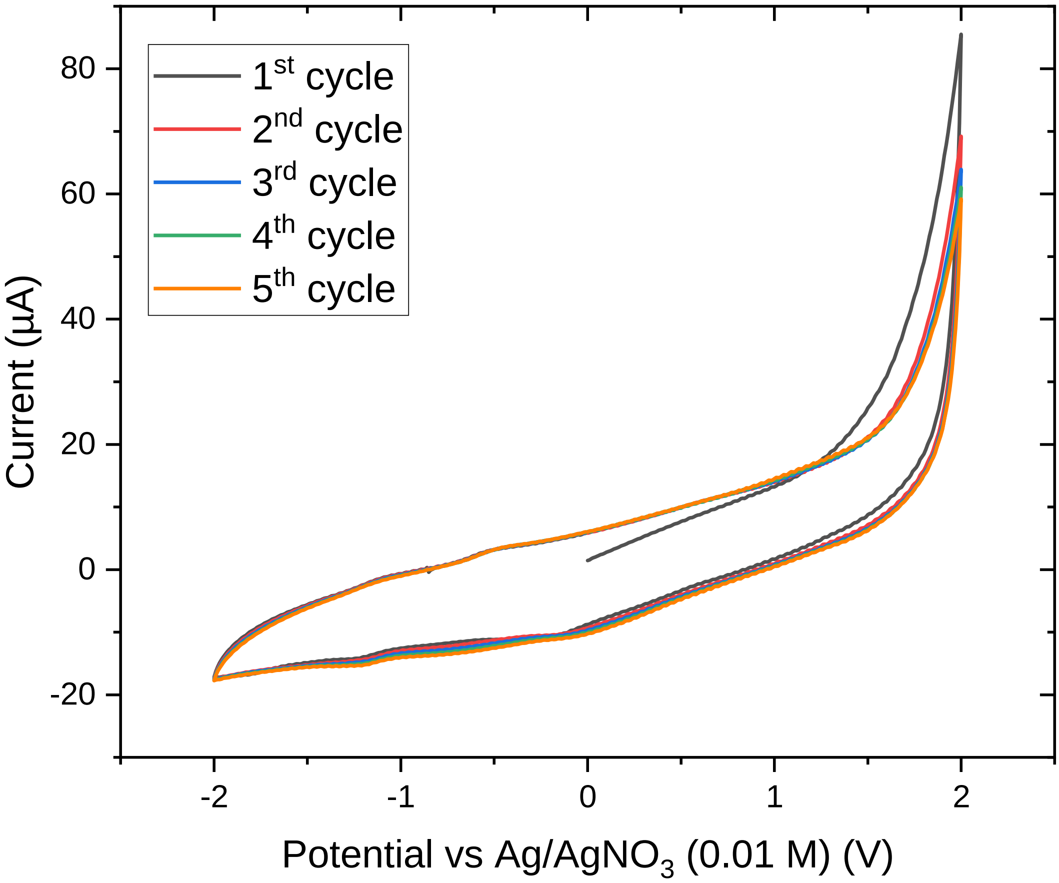

Figure S46. (Top) Five cycles of pretreatment CVs, 0→ 2→ -2→ 0 V vs 0.01 M $AgNO_3$/Ag, for a 0.1 M $(NBu_4)PF_6$ MeCN solution, with a glassy carbon working electrode (d = 3 mm, A = 0.071 cm2), scan rate 100 mVs^{-1}. See text for details and discussion.

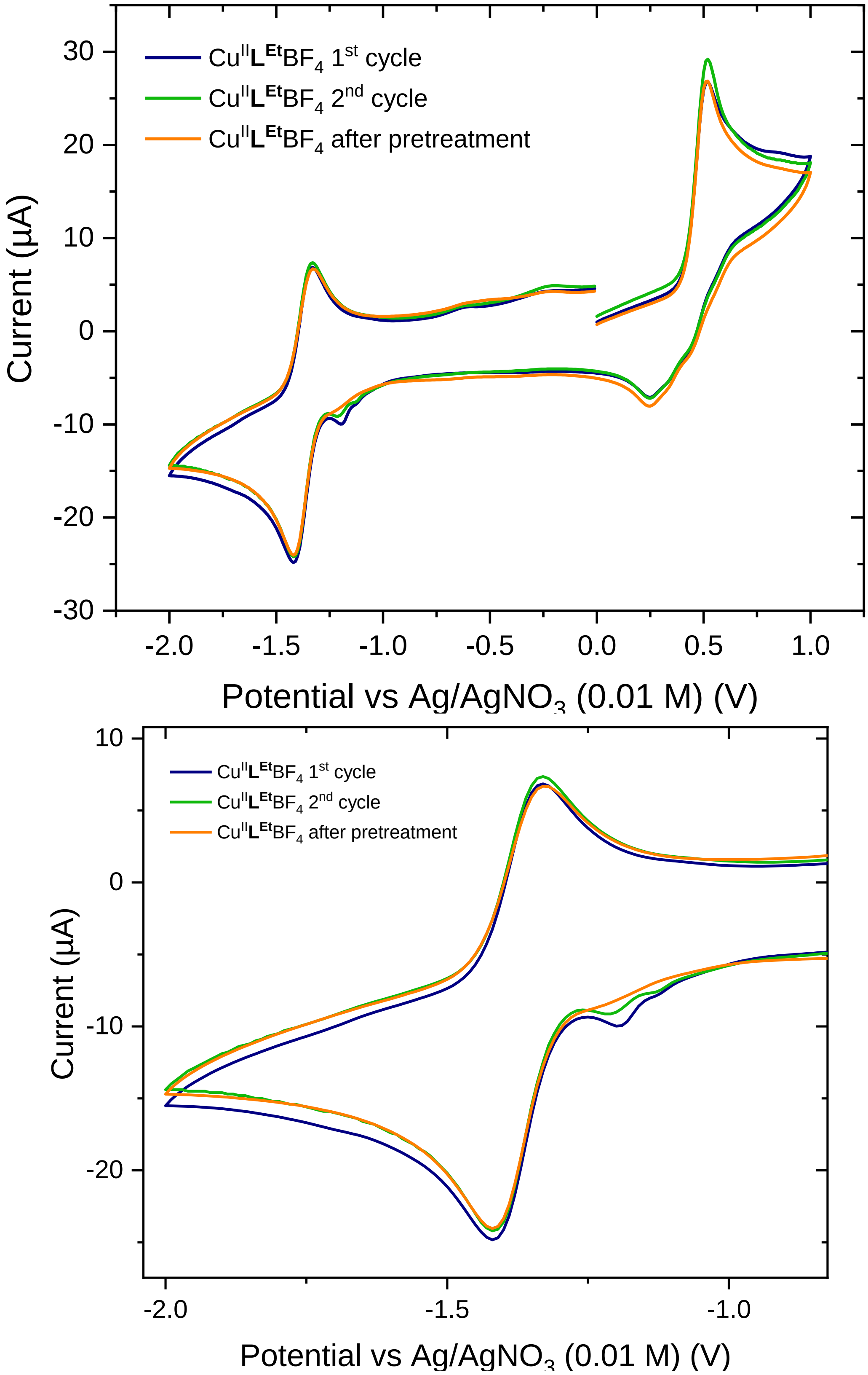

Figure S47. (Top) CVs, 0→ 1.0→ -2.0→ 0 V vs 0.01 M AgNO$_3$/Ag, for a 1 mM MeCN solution of [Cu^{II}**L**^{Et}]BF$_4$ 1st cycle (blue), 2nd cycle (green) and CV after treatment of the working electrode (details in text) as per the recommendations by Dempsey and co-workers[10] (orange). Conditions: 0.1 M (NBu$_4$)PF$_6$, glassy carbon working electrode (d = 3 mm, A = 0.071 cm2), scan rate 100 mVs^{-1}. (Bottom) zoom in on the 'bump' region.

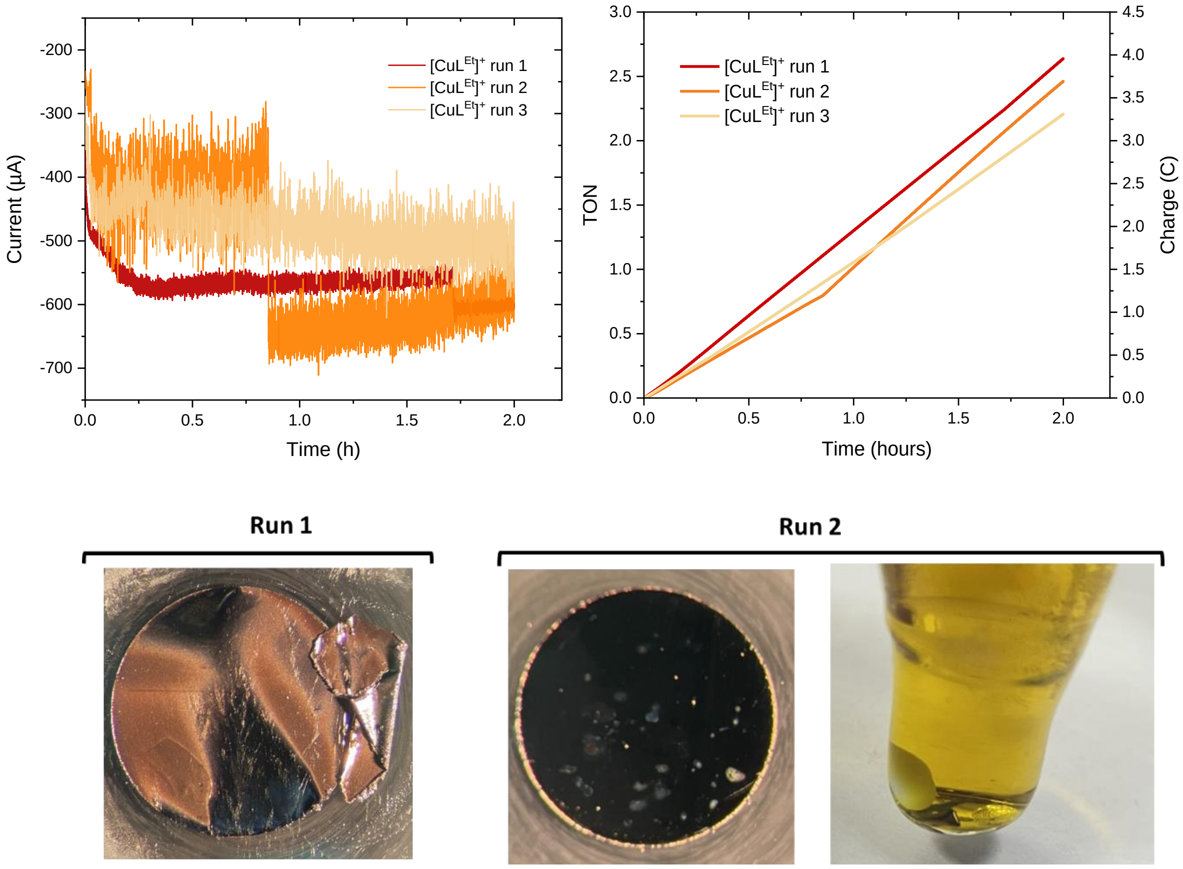

Figure S48. (Left) Multiple CPE experiments at −1.60 V of an 8 mL solution of 80 mM acetic acid in the presence of 1 mM of [Cu^{II}**L**^{Et}]BF$_4$ over 2 hours showing similar activity within experimental errors. (Right) The plot providing total charge transferred and TON for each CPE experiment. Conditions: 0.1 M (NBu$_4$)PF$_6$, glassy carbon working electrode (*d* = 3 mm, *A* = 0.071 cm^2), scan rate 100 mVs^{-1}. (Bottom) Glassy carbon electrode surface pictures showing visible deposit on the electrode surface, and working electrode deposits detached and settled at the bottom of the cell.

5 References

1. CrysAlisPro software, *Agilient Technologies,* Yarnton, Oxfordshire, UK, **2014**.
2. G. Sheldrick, Crystal structure refinement with SHELXL, *Acta Crystallogr., Sect. C*, 2015, **71**, 3-8.
3. O. V. Dolomanov, L. J. Bourhis, R. J. Gildea, J. A. K. Howard and H. Puschmann, OLEX2: a complete structure solution, refinement and analysis program, *J. Appl. Cryst.*, 2009, **42**, 339-341.
4. C. F. Macrae, I. J. Bruno, J. A. Chisholm, P. R. Edgington, P. McCabe, E. Pidcock, L. Rodriguez-Monge, R. Taylor, J. van de Streek and P. A. Wood, Mercury CSD 2.0 - new features for the visualization and investigation of crystal structures, *J. Appl. Crystallogr.*, 2008, **41**, 466-470.
5. S. K. Das and J. Frey, Regioselective double Boekelheide reaction: first synthesis of 3,6-dialkylpyrazine-2,5-dicarboxaldehydes from dl-alanine, *Tetrahedron Lett.*, 2012, **53**, 3869-3872.
6. T. K. Ronson, J. Nelson, G. B. Jameson, J. C. Jeffery and S. Brooker, Controlled access to mixed-metal pyridazine-linked cryptates, *Eur. J. Inorg. Chem.*, 2004, 2570-2584.
7. S. Brooker, J. D. Ewing, T. K. Ronson, C. J. Harding, J. Nelson and D. J. Speed, Redox-adaptable copper hosts; pyridazine-linked cryptands accommodate copper in a range of redox states, *Inorg. Chem.*, 2003, **42**, 2764-2773.
8. S. Brooker, J. D. Ewing, J. Nelson and J. C. Jeffery, Heterobinuclear cryptates; cooperative binding generates two different coordination sites within a symmetrical cryptand, *Inorg. Chim. Acta*, 2002, **337**, 463-466.
9. P. Zanello, *Inorganic Electrochemistry: Theory, Practice and Application*, Royal Society of Chemistry, Cambridge, UK, 2003.
10. N. Elgrishi, K. J. Rountree, B. D. McCarthy, E. S. Rountree, T. T. Eisenhart and J. L. Dempsey, A Practical Beginner’s Guide to Cyclic Voltammetry, *J. Chem. Ed.*, 2018, **95**, 197–206.
11. A. M. Abudayyeh, M. S. Bennington, J. Hamonnet, A. T. Marshall and S. Brooker, Copper-based Electrocatalyst for Hydrogen Evolution in Water, *Dalton Trans.*, 2024, **53**, 6207 - 6214.
12. A. M. Abudayyeh, O. Schott, G. S. Hanan and S. Brooker, Copper catalysts for photo- and electro-catalytic hydrogen production, *Inorg. Chem. Front.*, 2021, **8**, 1015-1029.
13. R. Sanyal, S. A. Cameron and S. Brooker, Synthesis and complexes of an N_4 Schiff-base macrocycle derived from 2,2’-iminobisbenzaldehyde, *Dalton Trans.*, 2011, **40**, 12277-12287.